3. a-Si:H to nc-Si:H transition

Improved performance has been attributed to a-Si:H deposited near the transition to nc-Si:H. In this chapter, the influence of different deposition parameters on the crystallinity of the material, and consequently, on its optoelectronic properties, is analysed. The transition from a-Si:H to nc-Si:H is studied after variation of either the filament temperature, the process pressure or the hydrogen dilution. Finally, the mechanisms leading to the observed microstructural changes are discussed.

3.1. a-Si:H on the onset of microcrystallinity

The beneficial role of hydrogen dilution in PECVD deposited a-Si:H has been widely accepted since observations of improved stability were first reported [Guha et al 1981]. Moderate hydrogen dilutions (lower than those used in PECVD) have also led to reduced defect metastability in a-Si:H obtained by Hot-Wire CVD [Bauer et al. 1998b]. Not only improved material properties have been obtained after hydrogen dilution, but also enhanced stabilized performance of a-Si:H based solar cells has been achieved in both PECVD and Hot-Wire CVD [Xu et al. 1996, Tsu et al.1997, Bauer et al. 1998, Guha et al.1999, Yue et al. 2000, Guha et al. 2003]. Thus, a-Si:H obtained just before the onset of microcrystallinity has yielded the most stable solar cells. Improved order, etching of weak bonds, and lower hydrogen content (C_H) seemed to account for the observed improvement. On the other hand, recent results on nc-Si:H solar cells grown by both PECVD and Hot-Wire CVD have also focused attention on that material obtained near the transition edge between a-Si:H and nc-Si:H [Vetterl et al. 2000, Klein et al 2002]. Furthermore, a variety of thin film silicon materials produced near the onset of crystallisation, which exhibit very promising properties, have gained interest during the last years. Thus, polymorphous silicon (pm-Si:H) [Roca i Cabarrocas et al. 1998] or protocrystalline silicon (pc-Si:H) [Koh et al. 1999, Fontcuberta i Morral and Roca i Cabarrocas, 2001] are new terms that have been recently introduced into the terminology of thin film silicon technology.

The above-mentioned results clearly point to the necessity of a clear evaluation of the effect of the different technological parameters on the crystallinity of thin film silicon

layers obtained by Hot-Wire CVD. Microstructure features have been typically varied by means of properly tuning hydrogen dilution (D_H) and/or substrate temperature (T_s) [Tsu et al. 1997, Bauer et al. 1998b, Mahan et al. 2000, Han et al. 2003], though some questions arise regarding the role of other technological parameters such as the filament temperature (T_f) or the process pressure (P). In the following sections, microstructural properties as a function of the above-mentioned parameters (T_f, P, D_H and T_s) will be analysed. Substrate temperature was kept in the range of 200ºC, except when evaluating its own influence, as this regime allows the use of low cost substrates such as polymer foils [Alpuim et al. 2000], which we expect to employ in the future. In fact, preliminary results concerning the growth of transparent conductive oxides (TCO) on plastic substrates have already been presented by our group [Escarré et al. 2004].

3.2. Influence of filament temperature

In this section, results concerning the evolution of microstructural properties of thin silicon films after T_f variation will be presented. Structural properties depend critically on the growth precursors, which are influenced by the radicals emerging from the filament. In that sense, T_f plays a key role, as its value determines the decomposition efficiency per silane collision (α_{dec}) and the nature of the released radicals after the catalytic reaction.

A significant concentration of atomic hydrogen (H) near the growing surface has been identified as a critical parameter for the growth of nc-Si:H [Godet et al. 1995, Solomon and Drévillon 1993]. In fact, Hot-Wire CVD has been proved to be especially effective in the production of nc-Si:H (when compared with PECVD), as the filament itself acts as a very effective source of atomic hydrogen. This fact allows the deposition of nc-Si:H with no hydrogen dilution (differently from PECVD where a certain amount of H_2 is necessary), as we will see in this section.

As far as our study is concerned, a series of samples was grown at T_f ranging from 1600ºC to 1800ºC, whereas D_H = 0% and low substrate temperature (T_s = 200ºC) were employed. The T_f range was selected after taking into account those limitations linked to the filament properties. The use of too low temperatures (below 1500ºC) results in the rapid breakage of the filament due to the formation of silicides after Si atoms are bonded to metallic (M)

ones (M-silicides). High T_f leads to the desorption of Si atoms, so that the surface of the metallic wire returns to its original state. Nevertheless, at low T_f, the growth rate of the M-silicides might be faster that the Si atom desorption one, thus leading to increased brittleness [Matsumura et al. 2004]. On the other hand, too high T_f (above 2000ºC) can cause the incorporation of impurities in the sample [Horbach et al. 1991, Zedlitz et al. 1993] and the deformation of the wire after thermal dilatation. The mentioned T_f range is associated to the most commonly used tungsten filaments, whereas tantalum ones, which were in fact used in this section, seem to allow lower temperatures (down to 1300ºC) [Bauer et al. 1998, Van Veenendaal et al. 2001], but suffer from thermal deformation at T_f above 1900ºC. In summary, the deposition parameters used throughout the present section were those listed in Table 3.1.

T_s (ºC)	T_f (ºC)	P (mbar)	ϕ_{SiH4} (sccm)	D_H (%)
200	1600-1800	3.8×10^{-2}	4	0

Table 3.1. *Deposition parameters for samples deposited in the T_f series. The distance between the filament and the substrate ranged between 3 and 5 cm as an inverted basket geometry was selected.*

Regarding the filament characteristics, an inverted-basket shaped Ta filament as that shown in Fig. 3.1 was employed. The distance between the filament and the substrate ($d_{f\text{-}s}$), whose value plays a crucial role [Dusane et al. 1993], ranged between 3 and 5 cm for the top and bottom parts of the wire respectively, leading to a mean distance of around 4 cm.

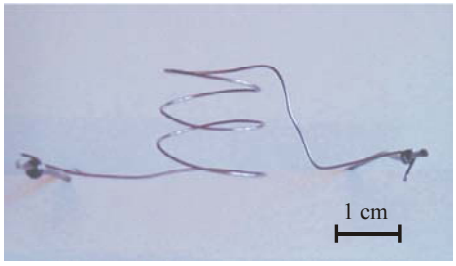

Figure 3.1. *Inverted-basket shaped Ta filament.*

Firstly, the thickness (d) and the deposition rate (r_d) for samples under study were measured (Table 3.2). Only a slight increase in r_d can be appreciated as T_f varied from 1600ºC to 1800ºC, giving evidence of only slightly enhanced α_{dec}.

T_f (ºC)	d (μm)	r_d (Å/s)
1600	0.75	4.2
1650	0.75	4.2
1700	0.80	4.4
1750	0.80	4.4
1800	0.80	4.4

Table 3.2. *d and r_d for samples considered in the T_f series.*

Structural features were first analysed by means of Raman spectroscopy, from which the crystalline fraction could be evaluated. Raman spectra as a function of T_f in the region studied are plotted in Fig. 3.2.

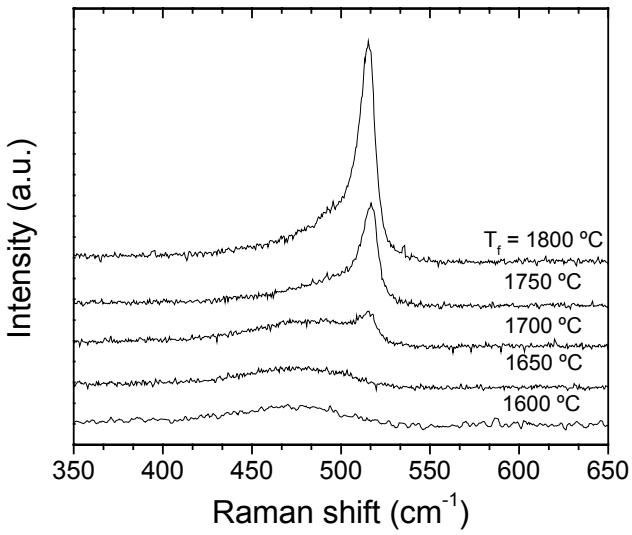

Figure 3.2. *Raman spectra for samples deposited at different T_f showing increasing X_c as T_f was varied from 1600ºC to 1800ºC.*

Raman spectra of samples grown at $T_f \geq 1750$ºC exhibited a clear contribution at 520 cm^{-1}, indicating an important nanocrystalline character. Crystalline fractions above 0.6 were obtained for these samples. On the contrary, purely amorphous layers were grown at $T_f \leq 1650$ºC, for which only a broad band around 480 cm^{-1} could be distinguished. Regarding that sample deposited at intermediate filament temperatures ($T_f = 1700$ºC), a two-phase material ($X_c \sim 0.12$) was obtained indicating incipient crystallinity.

Consistent results were obtained by FTIR spectroscopy as seen in Figure 3.3. A dominant contribution around 2000 cm^{-1} was observed for samples deposited at $T_f \leq 1650ºC$, pointing to an important fraction of hydrogen atoms bonded in monohydride bonds, SiH, and surrounded by a dense network. On the other hand, an increasing contribution around 2100 cm^{-1} was obtained for samples grown at $T_f \geq 1700ºC$, indicating the presence of either multihydride (SiH_2 or SiH_3) or monohydride bonds in a porous structure. The important contribution around 2100 cm^{-1} has been commonly associated to low-quality a-Si:H or nc-Si:H, as most hydrogen atoms in nc-Si:H are bonded at grain boundaries, where they are on the surface of crystallites facing intergrain voids. Besides, C_H, deduced from the absorption band at 630 cm^{-1}, decreased from ~ 12% to ~ 7% as T_f ranged from 1600 to 1800ºC, this being an additional indication of crystalline growth [Han et al. 2003].

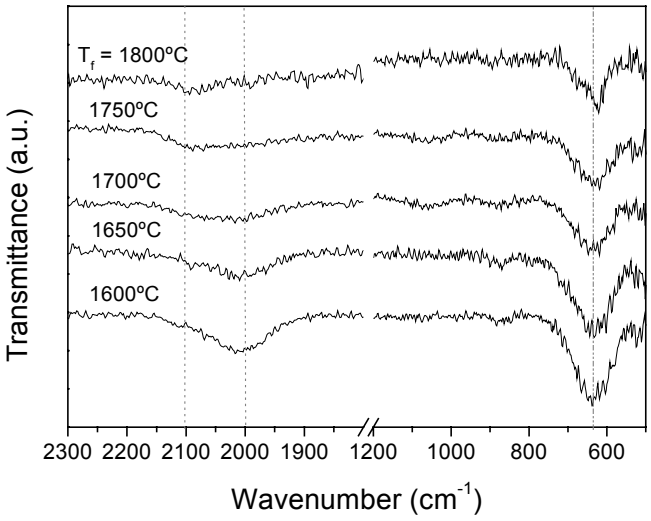

Figure 3.3. *FTIR spectra for samples deposited at different T_f showing increasing contribution at 2100 cm^{-1} and decreasing C_H as T_f was varied from 1600ºC to 1800ºC.*

Both Raman and FTIR spectra showed that the T_f variation was enough to clearly affect the microstructural properties. Moreover, it is worth remarking that equivalent results were observed when either electrical or optical properties were considered (Fig. 3.4). Both the activation energy (E_A) and the dark conductivity at room temperature (σ_d) were coherent with the structural characterization, as they also attested the existence of a transition as T_f approached 1700ºC. However, electrical properties at 1700ºC seemed to be mainly dominated by the crystalline contribution, even though a measurable amorphous fraction ($X_c \sim 0.12$) was evidenced by Raman spectroscopy measurements.

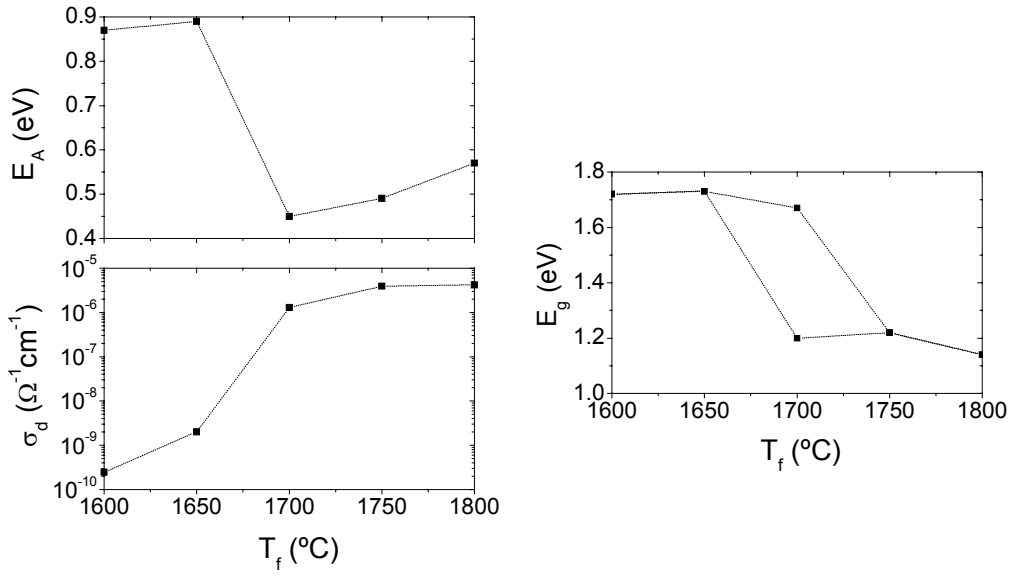

a) *b)*

Figure 3.4. *Electrical properties (a) and optical band gap (b) of thin silicon films as a function of T_f. In the transition zone, both amorphous and nanocrystalline optical absorption edges were observed.*

In order to clarify the electrical behaviour observed at intermediate filament temperatures, a typical TEM image corresponding to a two-phase material is presented in Figure 3.5.

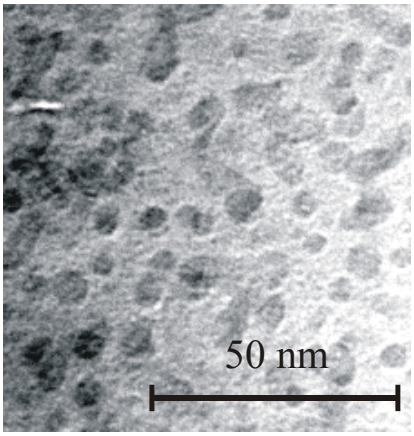

Figure 3.5. *TEM image of a two-phase material where crystallites (dark grey spots) are embedded in an amorphous tissue (light grey).*

The relationship of the mean distance between crystallites and the diffusion length of carriers plays a very important role when determining the electrical properties of the material. Crystalline properties can be observed when crystallites are close enough, which

seemed to be our case at X_c values as moderate as 0.12. Conversely, an abrupt transition to amorphous conduction is expected when the separation between crystalline grains becomes larger, so that conduction becomes dominated by the amorphous tissue surrounding them.

Clearer insight into the observed mechanism is given by the effective medium approximation (EMA), which allows the study of the properties of inhomogeneous materials [Stroud 1975]. A simplified vision will be employed in our case just to bring some light. Thus, thin silicon films will be considered as a random mixture of both crystallites and a-Si:H spherical shaped grains exhibiting volume fractions *f* and *1-f* respectively. More accurate studies would require the presence of a third medium (void) and the analysis of the actual geometry, that is, crystalline silicon grains embedded in an amorphous matrix. Thus, although qualitatively correlated, *f* and X_c can not be quantitatively compared. Anyhow, an effective conductivity (σ^{eff}) combining the conductivities of a-Si:H and crystallites can be extracted in this simplified case [Stroud 1975] as seen in eq. 3.1

$$f\frac{\sigma_a-\sigma^{eff}}{\sigma_a+2\sigma^{eff}}+(1-f)\frac{\sigma_c-\sigma^{eff}}{\sigma_c+2\sigma^{eff}}=0 \qquad (3.1)$$

The conductivity of bulk single-crystal Si (c-Si) might have been expected to be used in equation 3.1 for σ_c, but the finite size of the microcrystallites affects σ^{eff} (as also observed when the pseudoelectric function, ε, is evaluated [Kang et al. 2002]). Consequently, $\sigma_c = 10^{-6}\ \Omega^{-1}cm^{-1}$, this value corresponding to samples with very high crystalline fractions, was chosen. Figure 3.6 shows the evolution of σ^{eff} as a function of *f*, where a percolation threshold value is observed around 0.33 in agreement with different reported results [Kovácik 1998, Stroud 1998, Shimakawa 2000]. Thus, regions (grains) exhibiting high conductivity are small and isolated at low crystalline fractions, whereas with further increase in *f*, these regions start to interconnect until the critical (or threshold) *f* is reached. At this point, high conductivity regions establish some kind of high conductivity network throughout the entire layer, thus leading to high effective conductivity [Kovácik 1998].

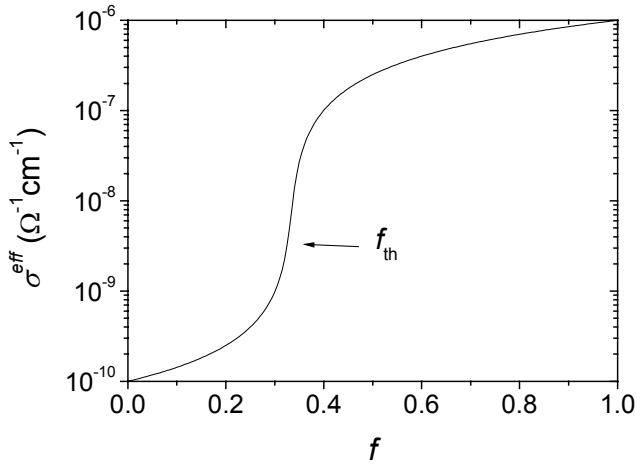

Figure 3.6. *σ^{eff} as a function of f evidencing an abrupt transition around f_{th}. $\sigma_a = 10^{-10}\ \Omega^{-1}cm^{-1}$ and $\sigma_c = 10^{-6}\ \Omega^{-1}cm^{-1}$ were chosen as typical values.*

Regarding optical properties, E_g (Fig. 3.4(b)) exhibited a clear amorphous character for T_f below 1650ºC, showing an average value of 1.7 eV. On the other hand, at T_f above 1750ºC, the optical properties evidenced the nanocrystalline behaviour of the samples, in agreement with their structural properties. In the transition zone, both amorphous and nanocrystalline absorption edges were observed, as the material consisted of a mixture of both phases ($X_c \sim 0.12$), each being dominant at a different energy range.

In order to analyse the presented results, both the SiH_4 decomposition efficiency and the nature of the released radicals must be considered. As far as α_{dec} is concerned, only a slight increase seemed to occur in our case, as deduced from the subtle change observed in r_d (from 4.2 Å/s at 1600ºC to 4.4 Å/s at 1800ºC). In that sense, the correlation between r_d and T_f was not as straightforward as that reported by other groups [Matsumura 1986, Horbach et al. 1991]. The SiH_4 decomposition efficiency on a metallic filament (tungsten in this case) was first analysed by [Doyle et al. 1988], whose results pointed out a clear dependence of α_{dec} on T_f. Some years later, a similar study was performed by [Horbach et al. 1991] at higher T_f. Both experiments showed that high T_f led to enhanced SiH_4 decomposition. Different hydrogen coverage of the wire was pointed as the main reason leading to such behaviour. Thus, high T_f values led to rapid hydrogen evaporation after absorption of SiH_4, therefore allowing the filament to be "fresh" for new SiH_4 molecules. Nevertheless, that did not seem to be the dominant mechanism in our case, as r_d (directly

linked to α_{dec}) increased only slightly. This result might be correlated with our deposition parameters set and/or reactor design.

As far as the nature of the radicals emerging from the gas-filament reactions is concerned, they are known to affect the nature of the growth precursors. On one hand, some of the released species can reach the substrate without undergoing any collision, thus becoming growth precursors, whereas, on the other hand, secondary gas-phase reactions giving rise to different growth precursors can also occur [Molenbroek et al. 1997, Gallagher 2001]. Different studies identified H and Si as the radicals most effectively generated on the filament surface [Doyle et al. 1988, Duan et al. 2002b]. In fact, hydrogen can be effectively released from the wire, either as H_2 or H, for T_f values as low as 1200-1300ºC. On the other hand, Si atoms require higher energy to begin evaporating from the surface of the filament ($T_f \sim 1500$ºC). Higher T_f lead to enhanced production of Si until almost all Si atoms produced from absorbed SiH_4 molecules are evaporated at $T_f > 1800$ºC. Our results pointed to an increased production of atomic hydrogen as T_f was raised. H production at the filament is favoured as T_f is raised by limiting the formation of H_2 after combination of two H atoms. High T_f values lead to reduced hydrogen coverage of the surface and, though lower energy is required to evaporate H_2 than to release H, the need of proximity of two H atoms to form H_2 can only be satisfied at low T_f [Mahan 2003]. Not only enhanced concentration of H near the growing surface is achieved at high T_f, but also the production of high mobility species (such as SiH_3) is favoured by the presence of atomic hydrogen through the well-known reaction

$$H + SiH_4 \rightarrow SiH_3 + H_2 \qquad (3.2)$$

In summary, α_{dec} changed only slightly, so that selective favoured production of H at higher T_f seemed to be the main mechanism leading to nc-Si:H in agreement with reported results [Bourée 2001, Jadkar et al. 2003]. In particular, increased H/SiH_3 ratio between the fluxes of atomic hydrogen and SiH_3 radical on the growing surface at increasing T_f was reported by [Abe et al. 2000]. Alternative approaches, such as the use of large area wires leading to enhanced H production were expected to favour the growth of nc-Si:H. In fact, previously performed experiments [Peiró 1999] manifested a shift towards low T_f on the microstructure transition as the area of the filament was enlarged. Thus, two inverted-

basket shaped tungsten filaments with either five or six loops were employed. Moreover, studies performed with a simple linear filament exhibiting smaller area led to purely amorphous samples for T_f as high as 1850ºC.

3.3. Influence of pressure

Pressure is expected to influence the structural properties of silicon thin films through different mechanisms. High deposition rate leading to disordered and porous material is expected as *P* increases. Moreover, the mean free path (λ_{mfp}) of the involved species is affected by *P*, so that low λ_{mfp} is obtained at high pressures due to the increased density of molecules in the deposition chamber. Besides, it is known that secondary reactions in gas phase, which eventually determine the nature of the growth precursors, strongly depend on the relation between λ_{mfp} and $d_{f\text{-}s}$ [Molenbroek et al. 1997, Feenstra et al.1999].

Different wire geometries involving varying shapes and $d_{f\text{-}s}$ were used in this work. In this section, a detailed study was performed with an inverted-basket shaped tungsten filament (similar to that shown in Fig. 3.1). *P* was varied between 2.4×10^{-2} and 1.9×10^{-1} mbar according to the position of the butterfly valve of the reactor, whereas the rest of the deposition conditions were kept constant as listed in Table 3.3. In accordance with the *P* range under study, λ_{mfp} ranged from ~ 2 cm at $P = 2.4\times10^{-2}$ mbar to ~ 0.25 cm at 1.9×10^{-1} mbar, as deduced from

$$\lambda_{mfp} = k_B T / (\sqrt{2} \cdot \sigma_{coll} \cdot P) \tag{3.3}$$

where T is the gas temperature and σ_{coll} is the collision cross section. A gas temperature value of 500 K and σ_{coll} of 10 Å^2 were used [Perrin et al.1996].

T_s (ºC)	T_f (ºC)	P (mbar)	ϕ_{SiH4} (sccm)	D_H (%)
200	1640	2.4×10^{-2} - 1.9×10^{-1}	4	0

Table 3.3. *Deposition conditions in the P influence study. λ_{mfp} was varied between 2 and 0.25 cm.*

Both the thickness and the deposition rate for samples under study are listed in Table 3.4, where lower r_d at both ends of the pressure range under study can be observed.

P (mbar)	***d (μm)***	***r_d (Å/s)***
2.4×10^{-2}	*1.6*	*4.4*
3.8×10^{-2}	*2.5*	*6.9*
9.2×10^{-2}	*2.3*	*6.4*
1.1×10^{-1}	*2.7*	*7.5*
1.9×10^{-1}	*1.4*	*3.9*

Table 3.4. *d and r_d for layers analysed in the P influence study. Lower r_d was measured for samples deposited at both the lowest and the highest pressures.*

The influence of the process pressure on the structural properties was clearly manifested by both Raman and FTIR spectra (Fig. 3.7), as a clear transition from a-Si:H to nc-Si:H was observed at $P \sim 1\times10^{-1}$ mbar.

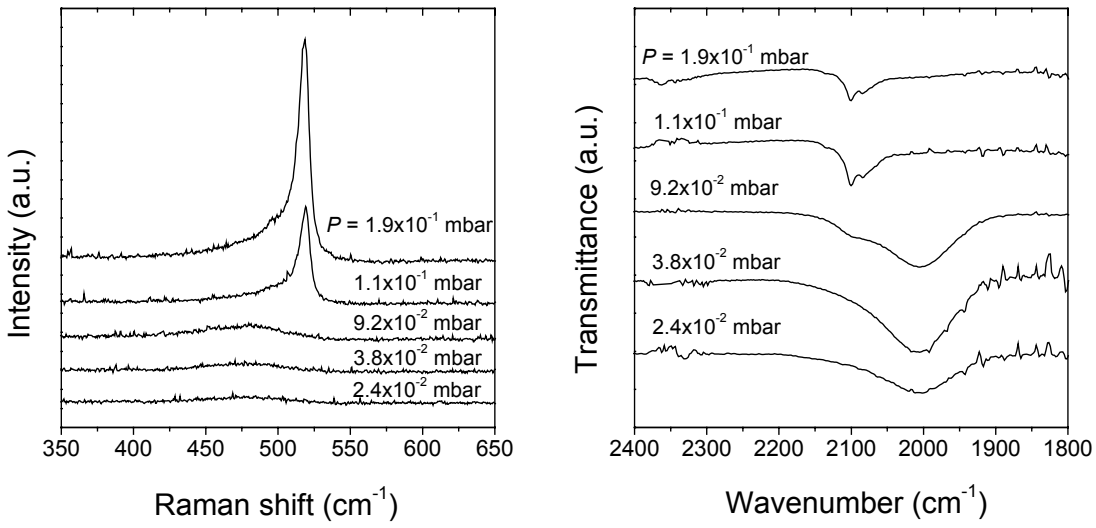

a) *b)*

Figure 3.7. *Raman (a) and FTIR (b) spectroscopy data as a function of pressure.*

As already observed in the T_f study, slight variations in the parameter under study induced very significant changes in the microstructure of the material. Accordingly, samples

deposited at $P = 9.2\times10^{-2}$ mbar exhibited a purely amorphous character, whereas a significant crystalline fraction was obtained at $P = 1.1\times10^{-1}$ mbar, thus evidencing a remarkably abrupt transition. Regarding FTIR data, an important absorption band around 2100 cm^{-1} was observed at $P = 1.1\times10^{-1}$ mbar, most probably due to the presence of hydrogen bonds at internal surfaces (mainly crystallites). On the other hand, only the absorption peak corresponding to monohydride bonds (2000 cm^{-1}) could be detected at $P \leq 3.8\times10^{-2}$ mbar. Furthermore, a measurable contribution around 2100 cm^{-1} could also be identified for that sample grown at $P = 9.2\times10^{-2}$ mbar, this being an indication of incipient microstructural changes at increasing pressures.

Once more, the optoelectronic properties of the material were clearly correlated with its microstructure. As an example, the Arrhenius plots of the dark conductivity corresponding to samples deposited at $P = 9.2\times10^{-2}$ and $P = 1.1\times10^{-1}$ mbar are presented in Fig. 3.8.

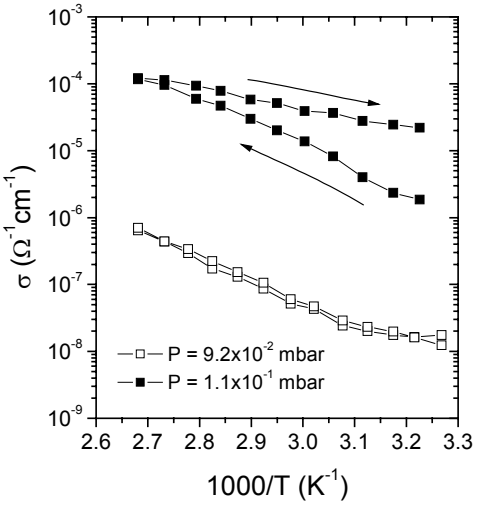

Figure 3.8. *Arrhenius plots of the dark conductivity, σ, for films deposited at $P = 9.2\times10^{-2}$ (a-Si:H) and 1.1×10^{-1} (nc-Si:H) mbar.*

The amorphous character of the sample deposited at $P = 9.2\times10^{-2}$ mbar could be clearly observed, as σ_d lay in the region of 10^{-8} $\Omega^{-1}cm^{-1}$, whereas $\sigma_d \sim 10^{-6}$ $\Omega^{-1}cm^{-1}$ was obtained at $P = 1.1\times10^{-1}$ mbar. On the other hand, E_A exhibited values of 0.84 and 0.61 eV for samples grown at $P = 9.2\times10^{-2}$ and 1.1×10^{-1} mbar respectively.

The deposition of nc-Si:H at high pressures might seem surprising, as low pressures are supposed to lead to a softer and gentler deposition process which might, eventually, give rise to a more ordered material. In fact, a transition from nc-Si:H to a-Si:H might not be discarded in our set-up if even higher pressures leading to very high deposition rates had been employed.

Studies dealing with the influence of P on the nature of the growth precursors have been published [Brogueira et al. 1996, Ichikawa et al. 2000]. The influence of P on the radical production is twofold. On one hand, the impingement rate of molecules on the filament can be expressed as $P/\sqrt{2\pi m k_B T}$ [Feenstra et al. 1999], where m is the molecular mass, k_B the Boltzmann's constant, T the gas temperature, and P the working pressure. Higher production of radicals is then obtained as P is increased and, in particular, higher concentration of atomic hydrogen leading to nanocrystalline growth in accordance with [Ichikawa et al. 2000] is expected. On the other hand, P has a clear influence on λ_{mfp}, whose relation with $d_{f\text{-}s}$ determines the number of secondary reactions and, consequently, the properties of the growth precursors [Dusane et al. 1993]. Experimental quantification of the importance of secondary reactions was performed by [Molenbroek et al. 1997]. Pressure was clearly observed to play a key role and, as a consequence, the product $P \cdot d_{f\text{-}s}$ was first introduced as an indicator of the number of gas-phase reactions. More details concerning this issue will be given in *Chapter 4*.

3.4. Influence of hydrogen dilution

Direct variation of the hydrogen dilution is the most immediate approach to modify the microstructure of the material. Different groups have reported a wide range of microstructures (from purely amorphous to polycrystalline silicon) after D_H changes [Brogueira et al. 1996, Heintze et al. 1996, Alpuim et al. 1999, Peiró 1999, Brüggermann et al. 2000, Han et al. 2000, Mahan et al. 2000, Bourée 2001, Levi et al. 2003]. Atomic hydrogen is effectively produced at the hot filament surface [Jansen et al. 1989], so that lower hydrogen dilutions than those commonly employed in PECVD are required to deposit nc-Si:H. In that sense, our group reported on the growth of highly crystalline material at low T_s and elevated hydrogen dilution by means of Hot-Wire CVD back in 1994 [Cifre et al. 1994].

D_H, whose value was varied between 0 and 95%, is defined as shown in equation 3.4. In our study, ϕ_{SiH4} was kept constant at 4 sccm, whereas ϕ_{H2} ranged from 0 to 76 sccm.

$$D_H = \phi_{H2} / (\phi_{H2} + \phi_{SiH4}) \tag{3.4}$$

The deposition conditions for samples grown in this section are listed in Table 3.5, whereas Table 3.6 shows the corresponding thicknesses and growth rates.

T_s (ºC)	T_f (ºC)	P (mbar)	ϕ_{SiH4} (sccm)	D_H (%)
200	1640	3.8×10^{-2}	4	0 - 95

Table 3.5. *Deposition parameters for samples grown in the D_H series. ϕ_{SiH4} was kept constant at 4 sccm whereas ϕ_{H2} was varied between 0 and 76 sccm.*

D_H (%)	d (μm)	r_d (Å/s)
0	1.1	4.1
50	0.9	3.3
75	0.8	4.4
95	0.4	1.1

Table 3.6. *d and r_d as a function of hydrogen dilution. A clear decrease in r_d for D_H = 95% is observed.*

A drastic reduction in r_d could be observed for that sample deposited at D_H = 95%. Etching of the growing surface due to atomic hydrogen reaching the substrate was pointed as a probable explanation for this result. Due to the etching selectivity (the etch rate of amorphous silicon by atomic hydrogen is higher than that for crystalline material), an important crystalline fraction was expected for that layer.

Raman spectroscopy results are plotted in Fig. 3.9, where the a-Si:H/nc-Si:H transition can be observed at approximately D_H = 75% (X_c around 0.12). Highly crystalline material (X_c ~ 0.65) was grown when dealing with D_H above 90%, whereas no contribution around 520 cm^{-1} could be observed at $D_H \leq 50\%$, indicating the absence of any crystalline growth.

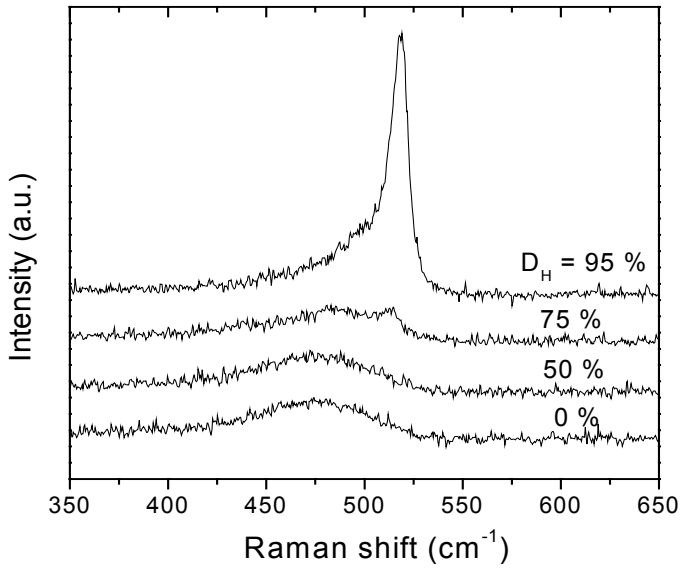

Figure 3.9. *Raman spectra as a function of D_H. Incipient crystallinity was obtained at D_H = 75%.*

In order to get additional information, the electrical properties of this series of samples were also analysed (Fig. 3.10). A clear transition was observed in both σ_d and *S* for $D_H \sim 75\%$ in accordance with the microstructural properties.

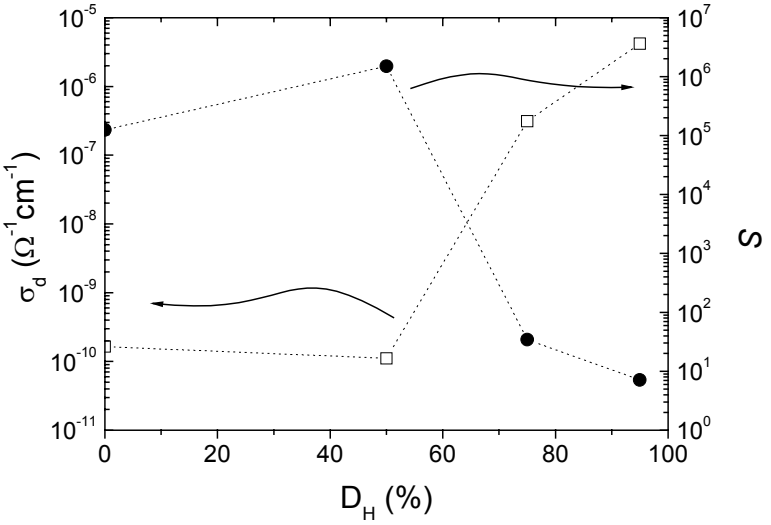

Figure 3.10. *σ_d and S as a function of hydrogen dilution.*

A similar result to that obtained in the study concerning the influence of T_f could be also observed. Thus, despite the moderate crystallinity obtained at D_H = 75% ($X_c \sim 0.12$), the

electrical properties seemed to be mainly determined by the crystalline phase. Therefore, and although neither σ_d nor *S* at D_H = 75% were the typical ones expected for nc-Si:H, their values showed the preponderance of the crystalline phase. Referring once more to Fig. 3.5, it seemed that the distance between crystallites was short enough as to prevent the amorphous tissue from determining the transport properties. In that sense, results reported by [Han et al. 2000] indicate that the onset of microcrystallinity is below the measurement limit of Raman spectroscopy, so that crystalline properties can be identified in optoelectronic properties even before any significant crystalline contribution appears in the Raman spectra.

In summary, and as already expected, D_H was observed to lead to enhanced production of H at the wire, so that the concentration of atomic hydrogen in the region close to the substrate was also favoured. It has been reported that the flux ratio H/SiH_3 is increased with D_H, causing the transition to nc-Si:H when the flux of H is large enough [Abe et al. 2000]. Furthermore, the use of hydrogen dilution can interestingly compensate for the utilisation of low substrate temperatures, so that nanocrystalline samples can be deposited at low T_s [Alpuim et al. 1999].

3.5. Influence of substrate temperature

The influence of the substrate temperature on the crystallinity of silicon thin films was also analysed. Although low substrate temperatures ($T_s \leq 200$ºC) were mainly employed in this work, the influence of T_s was also studied to get a deeper understanding of the deposition process. Nevertheless, only Raman spectroscopy results showing the microstructural properties of the deposited samples will be presented in this section.

The key role of H on thin silicon microstructure has been clearly demonstrated in previous sections. Anyhow, a different behaviour might be expected in this section, as two competing mechanisms coexisted in this case. On one hand, high T_s favours the surface mobility of growth precursors, thus leading to increased order and, eventually, crystalline growth. On the other hand, low H concentrations near the growing surface are expected as T_s is increased due to H desorption, this fact contributing negatively to the surface mobility.

Two different technological series, whose deposition parameters are listed in Table 3.7, were studied in this section. These series allowed us to correlate both the T_s and the D_H influence on the microstructural features.

Series	***T_s (ºC)***	***T_f (ºC)***	***P (mbar)***	***ϕ_{SiH4} (sccm)***	***D_H (%)***	***wire***
T_sA	*300-500*	*1550*	*1.0×10^{-2}*	*4*	*0*	*basket*
T_sB	*Heater off-500*	*1600*	*3.0×10^{-2}*	*4.5*	*93*	*linear*

Table 3.7. *Deposition parameters for samples deposited in the T_s series. No hydrogen dilution was used in the first series (T_sA), whereas D_H ~ 93% was selected for the second one (T_sB).*

No hydrogen dilution (D_H = 0%) was employed in the first series (T_sA), for which an inverted basket shaped Ta filament with three coils (Fig. 3.1) leading to r_d values around 5 Å/s was used. In previous sections, the ability of Hot-Wire CVD to produce nc-Si:H at such growth rates was already demonstrated. Besides, only high T_s values (≥ 300ºC) were considered in this study. Deposition conditions closer to the onset of the a-Si:H/nc-Si:H transition were employed in series T_sB. In particular, relatively high D_H and *P* values were selected, so that a more critical dependence on T_s than in the previous series was expected. Additionally, a linear Ta wire with $d_{f\text{-}s}$ ~ 4 cm was used in this case, which, in combination with the enhanced concentration of H, led to low r_d values (around 1.5 Å/s). It is important to remember that T_s values presented in Table 3.7 do not correspond to the actual temperature of the substrate, but to the set-point temperature ($T_{set\text{-}point}$) of the controllers. T_s is affected by radiation from the filament, especially when dealing with its lowest values as already mentioned in *Chapter 2* (section 2.1), so that our lowest temperature (with no heater) was actually around 125ºC. On the contrary, the upper limit (500ºC) corresponded in fact to T_s around 400ºC as also seen in section 2.1.

Information regarding the microstructural properties of the deposited layers was obtained by Raman spectroscopy. Purely amorphous material was obtained in series T_sA (Fig. 3.11), even when dealing with T_s as high as 500ºC. Similar results have recently been reported by different research groups [Han et al. 2003, Levi et al. 2003]. In this case, the amount of atomic hydrogen seemed to be insufficient to allow crystalline growth, despite the surface mobility was favoured by the high substrate temperatures employed.

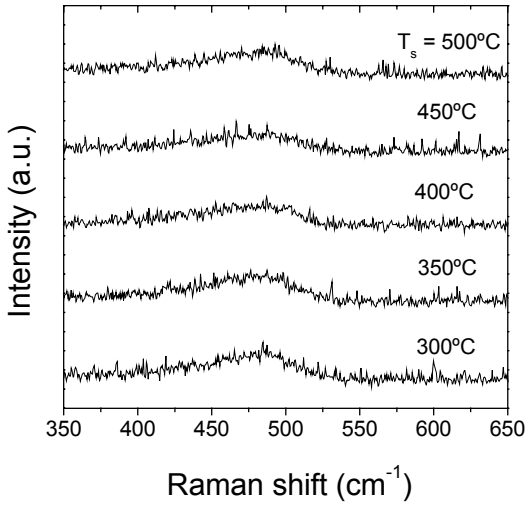

Figure 3.11. *Raman spectra as a function of T_s for series T_sA.*
No crystalline growth could be observed in this series, for which D_H = 0% was kept.

As far as series T_sB is concerned (Fig. 3.12), a different behaviour was observed. In this case, a clear transition to nanocrystalline growth could be observed at low T_s (125ºC), thus evidencing enhanced surface mobility.

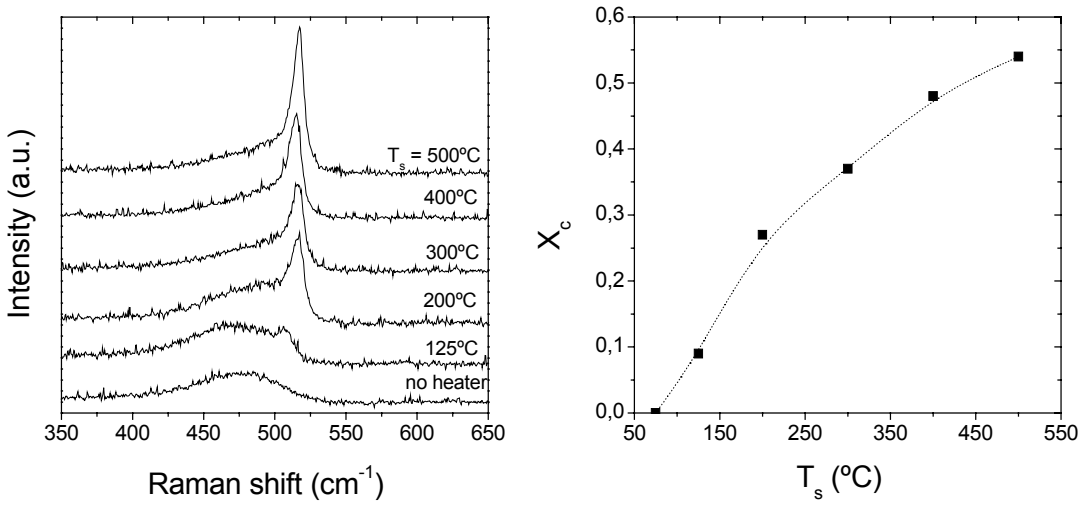

a) *b)*

Figure 3.12. *Raman spectra (a) and X_c values obtained from them (b) as a function of T_s for series T_sB.*
Enhanced crystallinity was obtained at increasing temperatures.

A D_H dependent threshold for T_s in the range under study seemed to exist for the transition a-Si:H/nc-Si:H. In particular, lower T_s values would be required at increasing D_H and vice versa [Han et al. 2003]. The evolution of X_c in this case is represented in Fig. 3.12(b), where higher X_c values are observed as T_s was varied from "room-temperature" ($X_c \sim 0$) up to 500ºC ($X_c \sim 0.55$). Purely a-Si:H was obtained at the lowest temperature under study, although a large concentration of atomic hydrogen was present in the deposition chamber ($D_H = 93\%$). In fact, this D_H value would have led to significant crystalline fractions if similar filaments to those used in section 3.4 had been employed. Nevertheless, enhanced crystallinity was easily obtained at moderate T_s values, pointing to an increased surface mobility of the growth species combining both the beneficial effect of increased T_s and a sufficient supply of atomic hydrogen on the growing surface.

3.6. Summary

Thin silicon films with microstructural properties ranging from purely amorphous to highly crystalline ($X_c > 0.65$) were obtained by properly tuning the different technological parameters. High filament temperature, pressure and/or hydrogen dilution allowed the deposition of highly crystalline material, even when dealing with relatively low substrate temperatures (T_s = 200ºC). In all cases, the enhanced production of atomic hydrogen was pointed as the fundamental mechanism leading to increased crystallinity. Atomic hydrogen leads to selective etching of the amorphous tissue and to enhanced diffusion of precursors due to coverage of the growing surface [Solomon and Drévillon 1993, Godet et al. 1995, Brogueria et al. 1996]. Additionally, the nature of the growth precursors was also expected to play a role, with high mobility species (such as SiH_3) leading to more ordered structures. In that sense, the flux ratio of species near the substrate ($[H]/[SiH_3]$ [Abe et al. 2000] or $[H]/[Si_xH_z]$ with $z \leq 3x$ [Brogueira et al. 1996]) has been proposed as an indicator in the literature, with high values leading to nc-Si:H and low values driving to the deposition of a-Si:H.

It is worth reminding that, in accordance with reported results, the transition from a-Si:H to nc-Si:H was remarkably abrupt, especially when the influence of either hydrogen dilution or pressure were analysed [Feenstra 1998, Levi et al. 2003], thus evidencing the drastic influence of the studied parameters on the microstructural features. Finally, it was proved

that an increase of the substrate temperature in the range under study (actual $T_s \leq 400$ºC) was insufficient to grow nc-Si:H, as long as the rest of the deposition parameters were not shifted to conditions favouring H production.

4. Intrinsic a-Si:H by Hot-Wire CVD

In this chapter, the required structural, electrical and optical properties of a-Si:H layers for their application in photovoltaic devices are presented. The influence of the deposition conditions on the material quality is evaluated and our state-of-the-art material is presented. Moreover, low substrates temperatures (below 200ºC) are employed throughout the study taking into account the future use of low-cost substrates.

4.1. Device-quality intrinsic amorphous silicon

Several features are required to intrinsic amorphous silicon (a-Si:H) for its incorporation as the active layer in photovoltaic devices. Although structural, electrical and optical properties can be individually analysed by means of different characterization techniques, a clear correlation between them is observed. In this section, the required features will be briefly summarized, whereas a deeper insight will be given in the forthcoming sections.

High absorption in the solar spectrum range allowing the maximum amount of electron-hole pairs to be generated is, obviously, one of the first requirements. The absorption coefficient (α) is expected to be above 3×10^4 cm^{-1} at 600 nm, whereas an optical band gap (E_g) in the range of 1.6-1.8 eV (depending mainly on the hydrogen content and microstructure properties) is expected. On the other hand, suitable transport properties are also required to collect the above-mentioned photogenerated carriers. Different parameters can be evaluated to determine the electrical properties of the samples, namely, the conductivity at room temperature (σ_d), the photoconductivity at standard illumination conditions (σ_{ph}), the photoresponse (*S*), or the mobility-lifetime product ($\mu\tau$) of carriers. Low σ_d values ($\sigma_d < 1\times10^{-10}$ $\Omega^{-1}cm^{-1}$) are demanded as an indication of the absence of electronically active impurities [Torres et al. 1996]. σ_d exhibits a thermally activated behaviour, whose activation energy (E_A) allows the determination of the Fermi level position, which should be around midgap. On the other hand, σ_{ph} is expected to reach high values (above 1×10^{-5} $\Omega^{-1}cm^{-1}$) indicating reasonably low recombination of the photogenerated carriers. $\mu\tau$ can be also determined from photoconductivity experiments, thus giving additional insight into the carrier transport properties. Anyhow, and despite the

fact that $\mu\tau$ deals with the properties of both minority and majority carriers, it is known that majority carriers play a dominant role due to its much longer lifetime. In particular, $\mu\tau$ values above 1×10^{-7} cm^2/V are required for device-quality material. Finally, *S* accounts for the electrical behaviour of the material both under illumination and dark conditions, being values above 10^5 desirable for the application of the material in solar cells. As far as the specific properties of minority carriers are concerned, they are known to play a critical role on the device performance. In that sense, large diffusion length ($L_D > 200$ nm) is needed to allow collection. The Steady-State Photocarrier Grating technique (SSPG) allows direct insight into the diffusion length of the minority carriers.

Although the influence of optical and electrical properties can be easily understood, structural features play a very important role too. Dense and compact material is required to prevent oxidation after air exposure, which clearly limits the device performance by modifying the properties of the material. Moreover, the above-mentioned electrical and optical properties are also affected by structural features. Thus, dense and "ordered" material is desired, as it exhibits improved optoelectronic properties. The demand for "ordered" material might seem surprising when dealing with a-Si:H, so it requires further explanation. It is known that amorphous silicon lacks long-range order, but its structure is highly ordered in the short range. As a matter of fact, that local order is responsible for the relatively similar properties of both crystalline and amorphous silicon. Accordingly, different "amorphous" materials can be deposited with different degrees of disorder in the long range. The expression "ordered" material refers then to those thin film layers exhibiting an atomic structure where local order is maintained to a certain degree beyond the first neighbours. Additionally, improved stability after long time exposure to light is required to prevent degradation due to the formation of metastable defects (Staebler-Wronski effect). In that sense, enhanced stability has been associated to a-Si:H grown near the transition to nc-Si:H in the literature [Xu et al. 1996, Bauer et al. 1998b], whose structure is supposed to exhibit enhanced order.

The properties required for device-quality a-Si:H have been summarized in Table 4.1, whose numerical values have been extracted from the literature [Street 1991, Schropp and Zeman 1998]. It must be mentioned that parameters in Table 4.1 correspond to optimum material, whereas solar cells with reasonable performance have been obtained when active

layers not fulfilling all the above-mentioned properties are used. In particular, the trend to increase the deposition rate (r_d) and decrease the substrate temperature (T_s), which usually implies the use of intrinsic layers with non-optimum properties, has recently focused great attention [Molenbroek et al.1997, Mahan et al. 2001, Van Veen and Schropp 2002].

	Property	***Requirement***
Structural properties	*density*	*high* $\Rightarrow$ *no oxidation*
	"order"	*high* $\Rightarrow$ *improved optoelectronic properties*
Electrical properties	σ_d	*low* $\Rightarrow$ $< 10^{-10}\ \Omega^{-1}cm^{-1}$
	σ_{ph}	*high* $\Rightarrow$ $> 10^{-5}\ \Omega^{-1}cm^{-1}$
	$\mu\tau$	*high* $\Rightarrow$ $> 10^{-7}\ cm^2/V$
Optical properties	E_g	*1.6 - 1.8 eV*
	absorption	*high* $\Rightarrow$ $\alpha(600\ nm) > 2\times10^4\ cm^{-1}$

Table 4.1. *Material properties for device-quality a-Si:H.*

4.2. Our intrinsic amorphous silicon

In the following sections, structural, electrical and optical features for our state-of-the-art material will be presented. These characteristics will be compared with the properties presented in section 4.1 and, besides, the correlation between different properties will be emphasized. Details regarding the deposition conditions and their influence on the material features will be given in section 4.3. Nevertheless, and as a first approach, it is worth mentioning that filament temperatures leading to a proper H generation ($T_f \sim 1600$ ºC for inverted-basket geometry), intermediate pressures (P between 1×10^{-2} and 4×10^{-2} mbar) and no (or very low) hydrogen dilution led to our state-of-the-art a-Si:H.

4.2.1. Structural properties

Different observations attest the influence of microstructural properties on the behaviour of intrinsic a-Si:H layers and on the performance of solar cells. Oxidation after air exposure,

stability after light soaking and initial optoelectronic properties have been shown to depend on the structure of deposited layers.

As a first requirement, high density is needed to prevent oxidation after exposure to atmosphere. Oxygen acts as an electronically active impurity that drastically worsens the transport properties of the material, so its diffusion into the bulk material must be minimized. Infrared spectroscopy measurements (FTIR) allow a direct identification of the oxygen incorporation into the film [Curtins and Veprek 1986]. Figure 4.1 shows the time evolution of FTIR spectra of two samples exhibiting different structural features.

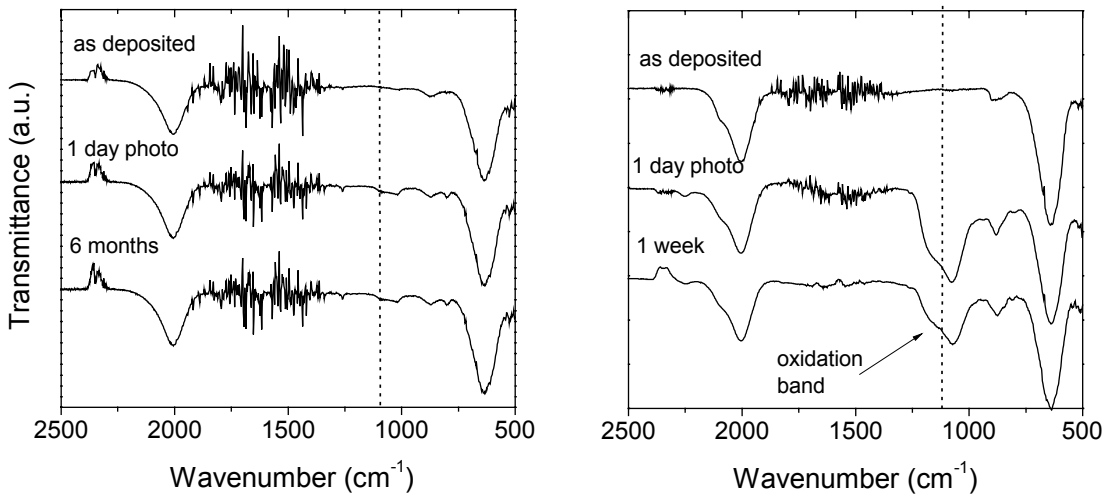

a) *b)*

Figure 4.1. *FTIR spectra of different a-Si:H layers. No oxygen incorporation was observed for our state-of-the-art a-Si:H (a), whereas low-quality material exhibited significant oxidation after either prolonged expose to air or just one day under illumination (photo) (b).*

The time evolution of the peak associated to Si-O groups clearly depended on the properties of the material. As seen in Fig. 4.1(*a*), samples with no detectable presence of oxygen even after several months of exposure to air were obtained. Conversely, enhanced oxidation after a few weeks or, more dramatically, after just one day under illumination, was confirmed for those samples exhibiting porous structures. Regarding measurements under illumination, impinging photons seemed to be responsible for the breaking of weak bonds (usually found in low-quality material), which eventually led to the incorporation of oxygen atoms into the growing structure.

Regarding FTIR data, valuable information could also be gained from the absorption bands around 2000 and 2100 cm^{-1} and the calculated microstructure factor (R^*) [Schropp and Zeman 1998]. R^* values around 0.1-0.15 are commonly required to incorporate the material into solar cells. Nevertheless, recent results have shown the ability to grow solar cells with reasonable conversion efficiencies, even with intrinsic layers exhibiting R^* between 0.2-0.3 [Van Veen and Schropp 2003]. In our case, three different spectra can be seen in Fig. 4.2, where a sample corresponding to our state-of-the-art is compared to two layers exhibiting increased disorder (all of them obtained at our laboratory).

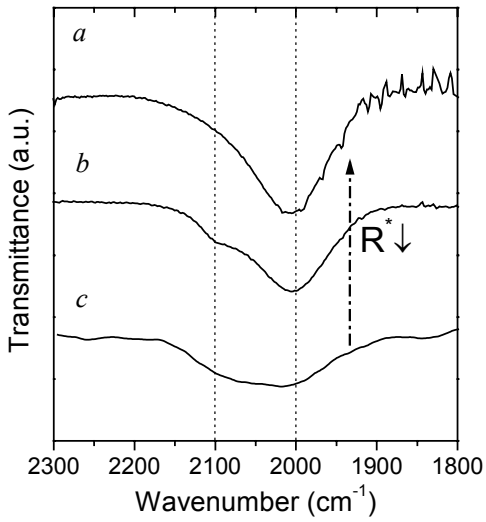

Figure 4.2. *FTIR spectra for a-Si:H films exhibiting different R^* values. Sample "a" corresponds to our state-of-the-art material whereas "b" and "c" correspond to low-quality material deposited at unsuitable conditions ("b" at too high pressure and "c" at too high filament temperature).*

R^* around 0.11 (± 0.01) was obtained for our state-of-the-art material (sample *a* in Fig. 4.2). The increased contribution around 2100 cm^{-1} observed in Fig. 4.2 for the other samples can be attributed to unsuitable deposition conditions. In this case, the use of a too high pressure (*P*) was responsible for the behaviour observed in sample *b*, whereas increased filament temperature (T_f), which in fact led to a detectable crystalline fraction (see *Chapter 3*), accounted for the contribution at 2100 cm^{-1} observed in sample *c*. Additional information can be obtained from the absorption bands situated between 800 and 900 cm^{-1}. These peaks correspond to hydrogen atoms bonded in multihydride configuration, which evidences a disordered structure. The increase of this contribution is

therefore related to the band centred at 2100 cm^{-1} as can be observed in Fig. 4.1(b), where increased absorption at 800-900 cm^{-1} can be appreciated for the porous sample.

As far as the total amount of hydrogen (C_H) is concerned, it can be evaluated from the absorption peak centred on 630 cm^{-1} [Langford et al. 1992]. In Fig. 4.3, the absorption coefficient is presented for our state-of-the-art material. C_H around 11% was observed, this value being close to those typically observed in PECVD material [Mahan et al. 1991, Schropp and Zeman 1998]. Much lower amounts of hydrogen leading to increased stability against light soaking have been reported [Mahan et al. 1991], although high T_s were employed (T_s > 400ºC) in those studies. Conversely, the use of low substrate temperatures (as in our case), favours the growth of highly hydrogenated material due to less hydrogen effusion from the substrate [Smith and Wagner 1987, Mahan et al. 1991, Van Veen 2003].

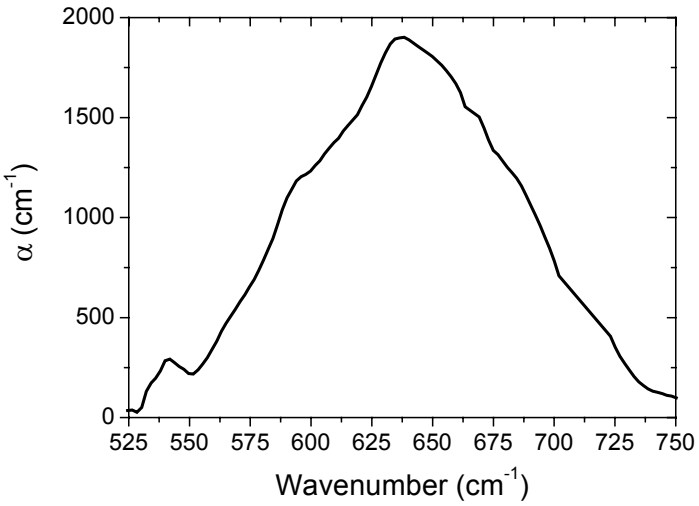

Figure 4.3. *Absorption band around 630 cm^{-1} for our state-of-the-art material.*

Valuable information was also provided by Raman spectroscopy, as proofs of a certain structural order in a-Si:H are given by this technique. Hence, the root-mean-square bond-angle variation ($\Delta\theta$) has been proposed as a measure of the degree of order [Beeman et al. 1985]. $\Delta\theta$ can be analysed by the observation of the transversal optic (TO) peak, associated to the Si-Si bond, which can be observed around 480 cm^{-1} for amorphous material and 520 cm^{-1} for crystalline one. In that sense, both the width of the TO peak (Γ) and its position have been proposed as an indication of $\Delta\theta$. Different models have been suggested [Beeman et al. 1985, Vink et al. 2001], where increased order (low $\Delta\theta$ values) is

characterized by a narrow band (low Γ) and a shift of the peak (ω_{TO}) toward high frequencies. Raman spectra for both a high-quality and a low-quality layer are plotted in Fig. 4.4.

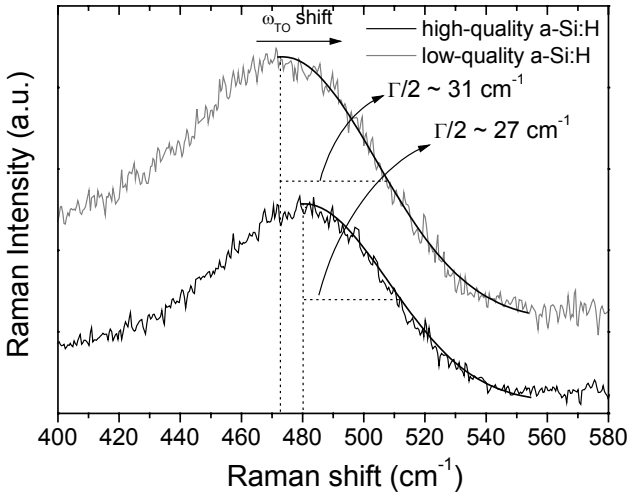

Figure 4.4. *Difference observed in Raman spectra (Γ and ω_{TO}) between device-quality a-Si:H and low quality films obtained at too high pressure (P ~ 1×10^{-1} mbar).*

As seen Fig. 4.4, Γ/2 at the high-energy side is given as a parameter instead of the full width, so that the influence of the longitudinal acoustic (LA) mode at 330 cm^{-1} and the longitudinal optic (LO) mode centred around 445 cm^{-1} can be avoided. Γ/2 below 30 cm^{-1} was observed for our state-of-the-art material, this value being fully comparable to those reported [Brockhoff et al. 1998, Jadkar et al. 2002]. According to different models, this Γ/2 value gives rise to $\Delta\theta$ values below 8º [Tsu et al. 1984, Beeman et al. 1985]. Regarding the peak position, its dependence on the material quality can also be observed in Fig. 4.4, where a shift (5-6 cm^{-1}) towards higher wavenumbers is observed for our optimised material. The mentioned shift can also be interpreted as a displacement towards the crystalline phase band (520 cm^{-1}). A similar trend has been observed after hydrogen dilution [Tsu et al. 1997, Han et al. 2003b], which is known to enhance stability [Guha et al. 1981, Bauer 1998b]. Besides, reported Transmission Electron Microscopy (TEM) measurements have shown the presence of small crystallites [Brokhoff et al. 1998] or linear like objects with some degree of order [Tsu et al. 1997], which seemed to account for the frequency shift and, eventually, for the improved microstructure.

High values of $\Delta\theta$ indicate the presence of strained bonds, which induce the formation of localized states near the band edges. These states give place to the so-called band tails in the optical absorption spectrum. Thus, a clear correlation can be found between $\Delta\theta$ and the Urbach slope (E_u) [Bustarret et al. 1988b]. Moreover, localized states in the band tails can be correlated to localized states in the mid-gap region (mainly due to dangling bonds) [Smith and Wagner 1987, Stutzmann 1989]. Optical measurements performed by means of Photothermal Deflection spectroscopy (PDS) are helpful to determine the structural order of the material through its influence on the Urbach front slope. Two different spectra are plotted in Fig. 4.5 corresponding to our state-of-the-art and to highly disordered material grown under unsuitable deposition conditions.

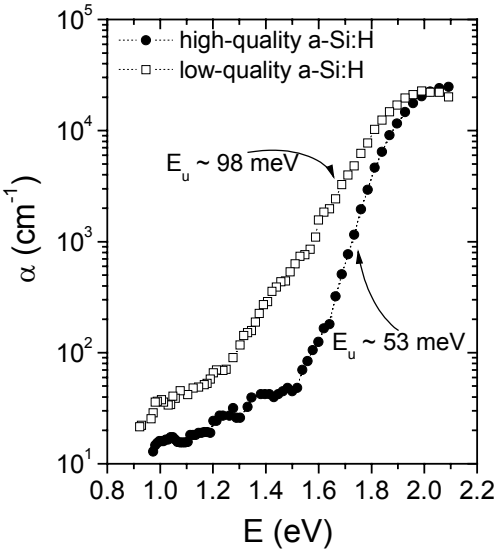

Figure 4.5. *PDS measurements of a-Si:H samples with different Urbach slopes indicating different degree of disorder. Different filament characteristics leading to different production of radicals on its surface were responsible for the change observed in this case.*

E_u values around 55 meV were deduced for our state-of-the-art material from the represented data. The obtained E_u values are acceptable and comparable to the ones reported by other research groups [Heintze et al. 1996, Alpuim et al. 1999], though they are slightly higher than those (< 50 meV) typically associated to PECVD device-quality a-Si:H [Stutzmann 1989]. In general, Hot-Wire CVD gives rise to broader absorption curves as measured by PDS than PECVD [Alpuim et al. 1999], therefore leading to higher E_u. Nevertheless, CPM measurements, which only account for bulk properties, result in

comparable E_u values for both PECVD and Hot-Wire CVD deposited samples. Consequently, Hot-Wire CVD material seems to have a larger surface defect density than PECVD obtained one [Papadopoulos et al. 1993]. In our case, the relatively high E_u could also be related to the use of low T_s ($\leq$ 200ºC).

The midgap density of states due to defects in the material (mainly dangling bonds) also contributes to light absorption in the low energy range. In that sense, absorption measurements below 1.2 eV approximately have been used to calculate the density of defects in the material [Jackson and Amer 1982]. For that purpose, PDS spectra can be employed, although some drawbacks arise from its use. In particular, PDS is known to be extremely sensitive to the presence of defects at both the front surface and the layer/substrate interface [Jackson et al. 1983]. This fact results in a clear dependence of the subgap absorption on the layer thickness [Ziegler 1997], thus making it difficult to distinguish between the contributions of the bulk and the surface.

Constant Photocurrent Method (CPM) allows the determination of subgap optical absorption without taking into account superficial effects, so more reliable results are consequently expected from this technique. CPM measurements of some of our samples were performed at the *Debye Institut* of the *Universiteit Utrecht*. Comparison between CPM and PDS spectra for the same sample can be seen in Fig. 4.6.

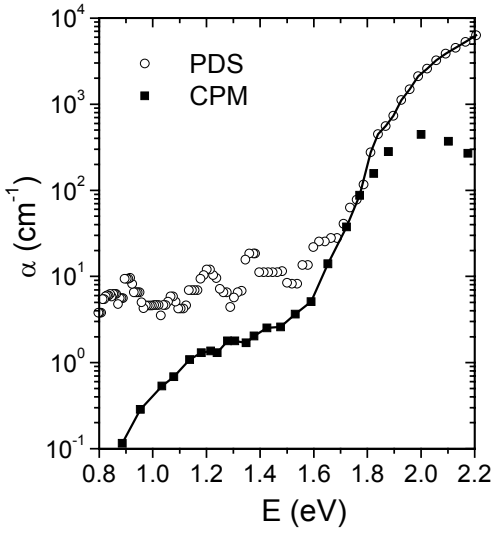

Figure 4.6. *PDS and CPM measurements of an a-Si:H sample indicating different subgap absorption. The solid line corresponds to the combination of PDS and CPM measurements.*

It is important to remark that the measured sample did not correspond to our state-of-the-art material, although the clear difference between CPM and PDS in the low energy range was clearly evidenced. In fact, the sample presented in this case exhibited lower N_d values than those observed in our best material. Unfortunately, very low photoconductivity impeded its use in photovoltaic devices. In that sense, defect densities (N_d) in the range of 5×10^{16} cm^{-3} (~10^{17} cm^{-3} as determined from PDS) were achieved for our best material, this being a slightly higher value than that observed in device-quality a-Si:H ($N_d < 1\times10^{16}$ cm^{-3}). This result is correlated with the E_u value, and could be associated with the high value of C_H (once more a consequence of the low T_s values used).

In summary, and as far as structural features are concerned, the most important results for our state-of-the-art a-Si:H are next enumerated:

1) a-Si:H resistant to oxidation diffusion after prolonged exposure to air was deposited indicating a compact structure.

2) Relatively high C_H around 11% seemed to be necessary to achieve high-quality material when keeping low substrate temperatures (T_s = 200ºC).

3) a-Si:H with quite an ordered structure was grown, i.e., low R^* values (~ 0.11), narrow Raman spectroscopy bands around 480 cm^{-1} ($\Gamma/2$ below 30 cm^{-1}), and E_u ~ 55 meV.

4.2.2. Electrical properties

Carrier transport properties have a dramatic influence on the solar cell performance, as proper collection of photogenerated pairs is required. The collection efficiency is affected by both the characteristics of the internal electric field (E_i) and the transport properties of the different layers involved in the structure, especially the active one. A clear connection between disorder and localized states in the mobility gap, which reduce the transport properties of photogenerated carriers, exists. On one hand, localized states in the band tails reduce the mobility of carriers through trapping and subsequent release. A relation was already proposed in 1970 [Le Comber and Spear 1970] to correlate the drift mobility (μ_D) and the mobility near the bottom of the extended states (μ_o). For electrons, and in the

simplest case of only one energetic level for localized states (at energy *E*), the next expression was found

$$\mu_D = \mu_0 \frac{N_C}{N_T} \exp\left[-\left(Ec - E\right)/kT\right] \tag{4.1}$$

where N_C and N_T represent the density of extended (non-localized) and localized states respectively near the mobility gap, and E_c corresponds to the upper limit of the mobility edge. Similar expressions to that presented in equation 4.1 can be applied to more realistic distributions of traps. Moreover, electronic properties can be reduced dramatically by recombination mechanisms, where both an electron and a hole recombine in a deep defect state. A schematic view of the band diagram including the localized states and their effect on transport properties can be seen in Fig. 4.7.

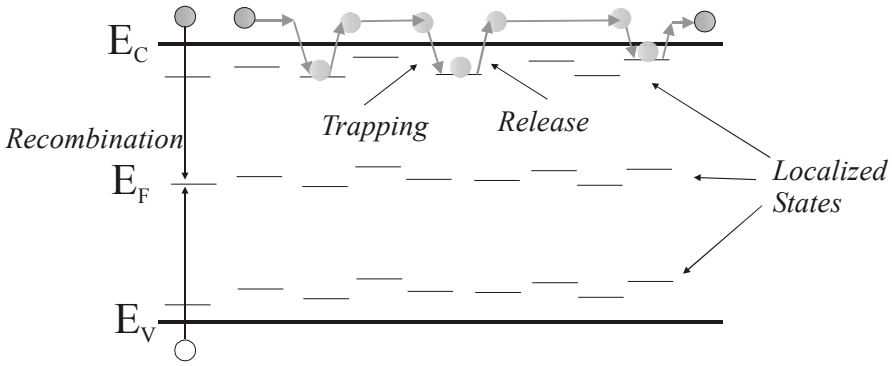

Figure 4.7. *Band diagram indicating the influence of localized states on the transport properties of generated carriers.*

Figure 4.8 shows σ(T) for our state-of-the-art and for a low-quality material obtained at unsuitable conditions (too high *P*). σ_d values between 5×10^{-11} and 2×10^{-10} $\Omega^{-1}cm^{-1}$ and activation energies between 0.8 and 0.9 eV were measured for our best a-Si:H. On the other hand, the low quality sample exhibited a too high σ_d value (~ 3×10^{-8} $\Omega^{-1}cm^{-1}$). In that sample, too high *P* seemed to have led to an increased void fraction, which might have resulted in the posterior oxidation. Unfortunately, oxygen is then expected to act as an electronically active impurity, thus limiting the device performance. E_A is expected to be around midgap for purely intrinsic material with no significant concentration of impurities,

as it corresponds to the distance between the Fermi level and the extended states band. It must be taken into account that even low impurity concentrations can significantly shift the Fermi level, thus reducing E_A. That seemed to be the case in our low-quality sample, for which $E_A \sim 0.46$ eV was determined.

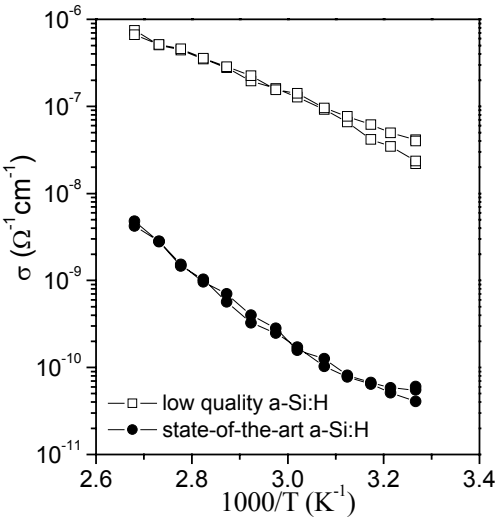

Figure 4.8. *Temperature dependence of the electrical conductivity for our state-of-the-art material (●) and a low quality layer (□).*

Some additional information can be gained from the shape of the Arrhenius curves. In particular, different conduction mechanisms are responsible for different regimes, which result in three temperature regions each one exhibiting a different slope [Le Comber and Spear 1970, Street 1991]. Extended state conduction is dominant at high temperatures, whereas conduction through hopping in either band tails or deep states near the Fermi level does also contribute as temperature is lowered. Thus, the evaluation of these contributions to the total conductivity gives some insight into the width of the band tails and the density of defect states in the midgap region. Nevertheless, temperatures involved in the present measurements only allowed the observation of transport through extended states. Additionally, relevant information is given by hysteresis effects [Street 1991], which are characteristic of disordered material. In that sense, two different curves are plotted in Fig. 4.9 for both low-quality and state-of-the-art material. Increased hysteresis is attributed to

increased concentration of localized states in the band tails, where carriers accumulate during the heating cycle.

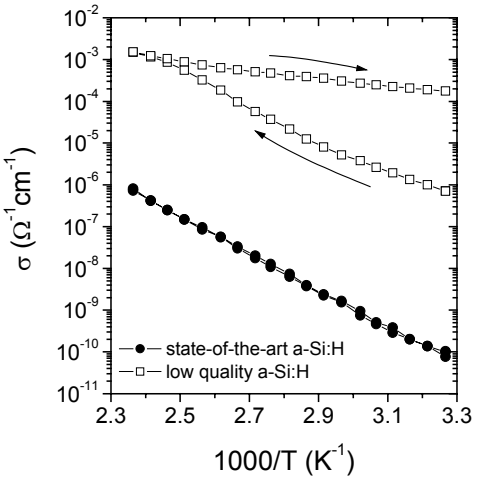

Figure 4.9. *Temperature dependence of the electrical conductivity evidencing hysteresis effects on low-quality a-Si:H.*

A relaxation process leading to the decay of the band tail carrier concentration causes the σ dependence on the thermal history of the sample. Fig. 4.10 shows the time evolution of σ_d evidencing the relaxation process.

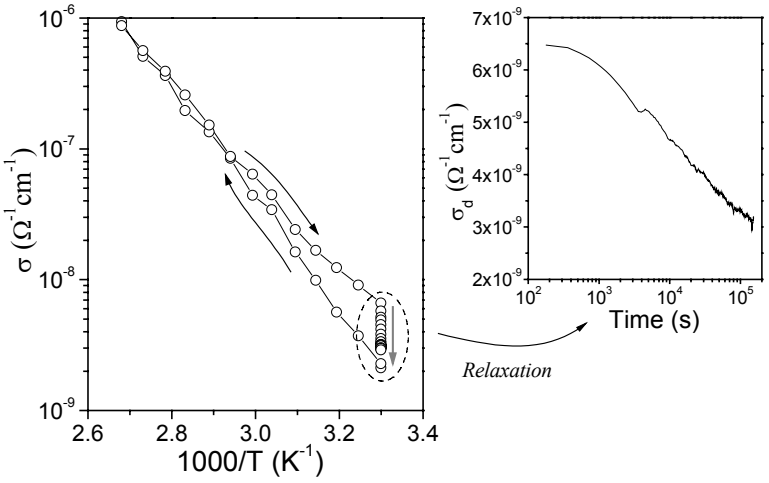

Figure 4.10. *Time dependence of σ_d showing the relaxation process.*

Regarding the response under illumination, Steady State Photoconductivity (SSPC) measurements were performed to determine σ_{ph}. This parameter as a function of the

generation rate (G) was analysed using a monochromatic light (λ = 620 nm), for which a uniform generation of electron-hole pairs can be expected when dealing with 1 μm thick samples. These experiments allowed the determination of the $\mu\tau$ of generated carriers [Ziegler 1997, Schropp and Zeman 1998]. In Fig. 4.11, a typical $\sigma_{ph}(G)$ curve for our device-quality intrinsic a-Si:H is presented. σ_{ph} was approximately proportional to G for the range under study. Nevertheless, it is known that a deviation from that behaviour can be observed when wider illumination ranges are employed, leading to a power dependence between σ_{ph} and G ($\sigma_{ph} \sim G^{\gamma}$).

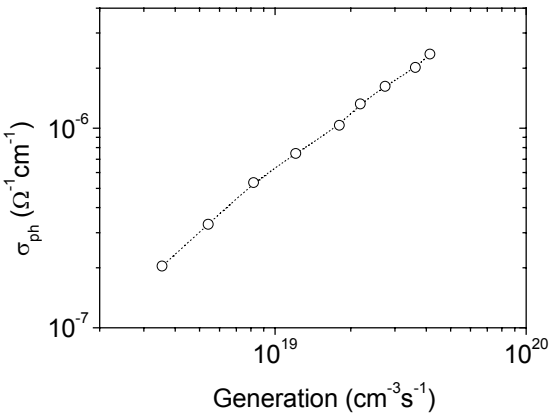

Figure 4.11. *σ_{ph} as a function of G for our state-of-the-art material.*

From photoconductivity measurements, $\mu\tau$ of majority carriers could be determined from

$$\sigma_{ph} = e\mu\tau G \tag{4.2}$$

In the ideal case, $\mu\tau$ does not depend on the illumination conditions, though the above-mentioned power relation between σ_{ph} and G causes $\mu\tau$ to vary with the generation rate. In our case, $\mu\tau$ was then evaluated at $G = 10^{21}$ cm^{-3}s^{-1}, corresponding to the expected generation rate under one sun illumination. $\mu\tau$ values above 1×10^{-7} V/cm^2 were usually achieved for our best material, though samples exhibiting $\mu\tau$ as high as 1×10^{-6} V/cm^2 were deposited. Anyhow, these layers exhibited also relatively high σ_d values (~ 10^{-9} Ω^{-1}cm^{-1}), which pointed to the presence of contaminants.

Regarding the value of σ_{ph} under standard illumination conditions (G = 10^{21} $cm^{-3}s^{-1}$), values above 5×10^{-5} $\Omega^{-1}cm^{-1}$ were achieved for our best material, which is expected to be large enough. Nevertheless, high σ_{ph} values under standard illumination conditions cannot be straightforwardly associated to device-quality a-Si:H, as they can be related to abnormally high values of σ_d. Therefore, both σ_{ph} and σ_d must be jointly considered. According to its definition, *S* above 10^5 are required [Schropp and Zeman 1998]. In our work, *S* values in the range of 5×10^5 were obtained for our state-of-the-art material combining both high σ_{ph} values and low σ_d values.

Finally, it must be considered that majority carriers (electrons in our case) show a major contribution to $\mu\tau$ [Voz 2001], so the transport features of minority carriers, which in fact limit the performance of solar cells, remain hidden. Different techniques allow the determination of minority carriers properties. SSPG deals with the ambipolar transport, which is mainly dominated by the mobility of the less mobile carriers, allowing the determination of their diffusion length (L_D). Measurements performed at the *Debye Institut* of the *Universiteit Utrecht* led to values above 200 nm for our state-of-the-art material, these values being compatible with the requirements for later implementation in solar cells.

4.2.3. Optical properties

The optical band gap (E_g) is one of the key parameters when determining the properties of a-Si:H. E_g between 1.6 and 1.8 eV are usually found in a-Si:H, this value depending on different material parameters, such as C_H [Cody 1981, Maley and Lannin 1987, Mahan 1991] or band tail width [Yamaguchi and Morigaki 1999]. As high α is achieved at energies near the optical band gap, transmittance (*T*) measurements are suitable for the determination of E_g. This situation appears as opposed to the absorption in the low energy region due to defects in the material, which gives rise to very low absorption coefficients. These low α values are best measured by means of highly sensitive techniques (PDS or CPM for example), which measure the absorptance of the sample (*A*). Thus, both *T* and *A* measurements must be complemented to fully acquire the optical absorption spectrum. Once *T* and *A* are measured, α over the whole range can be evaluated from

$$e^{\alpha d} = \frac{4ns\left(1+\frac{A}{T}\right)+\sqrt{\left[4ns\left(1+\frac{A}{T}\right)\right]^2+4\left(n^2-s^2\right)^2}}{2\left(n+s\right)^2} \tag{4.3}$$

where d is the thickness of the sample, and *n* and *s* are the refractive indexes of the film and the substrate respectively [Ritter and Weiser 1986, Voz 2001]. The measured absorption coefficient spectrum for one of our standard film is presented in Fig. 4.12.

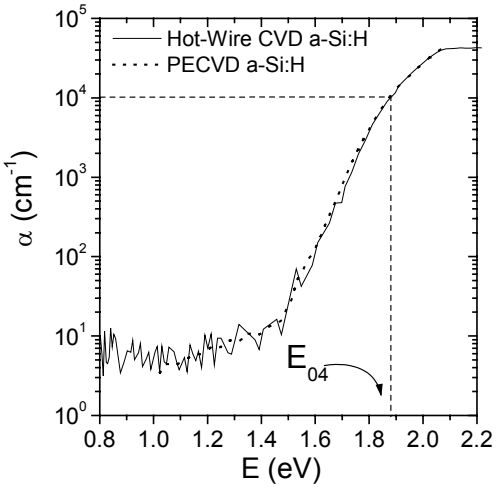

Figure 4.12. *α spectrum showing an abrupt increase as the energy reaches values near E_g.*

Once the above-represented spectrum is obtained, different approaches can be followed to analytically determine the value of E_g. Tauc's approach [Tauc 1974] considers parabolic band edges, so the next expression (Tauc's law) is proposed

$$\sqrt{\alpha h\nu} = A(h\nu - E_g) \tag{4.4}$$

On the other hand, if the distribution near the band edges is assumed to be linear [Klazes et al. 1982], a cubic dependence between the absorption coefficient and the energy emerges, which, in fact, seems to fit the spectrum over a wider range than the most commonly employed Tauc's law. In this case, the so-called cubic gap is obtained from

$$(\alpha h\nu)^{1/3} = A(h\nu - E_g) \tag{4.5}$$

The cubic relationship leads to E_g values that are 0.1-0.2 eV lower than those obtained with the Tauc's law. In Fig. 4.13, the determination of E_g for our state-of-the-art material has been presented using both approximations. Additionally, the energy value at which α reaches 10^4 cm^{-1}, E_{04}, which has been proposed as an alternative approximation to the band gap, has been presented in Fig. 4.12.

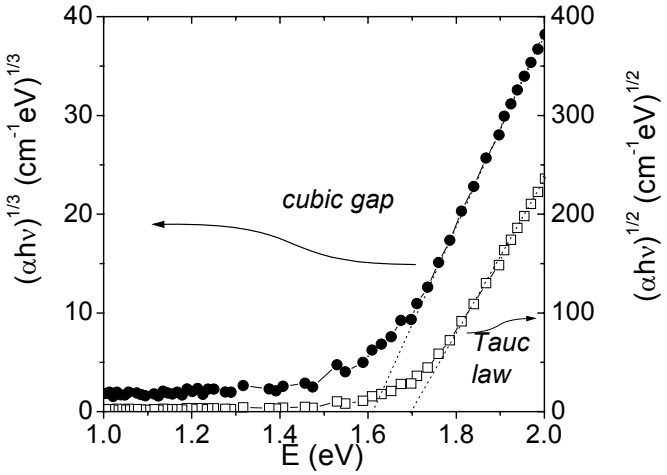

Figure 4.13. *Determination of E_g by means of the Tauc law and the cubic gap approximation.*

From the above-mentioned methods it can be clearly seen that not a clear definition of E_g can be given, so that it is important to clearly identify the method used. As seen in Fig. 4.13, $E_g \sim 1.70$ eV was determined from the Tauc's law, whereas a slightly lower value was obtained with the cubic gap approximation. From now on, the Tauc's law approach will be used, so a value of ~ 1.70 eV can be associated to our state-of-the-art material. Nevertheless, variations of ± 0.05 eV were easily observed for our high-quality material. The obtained value lies in the typical range associated to device-quality a-Si:H and was also consistent with the hydrogen content of our best material ($C_H \sim 11\%$) through the next expression [Papadopoulos et al. 1993]

$$E_g = 1.57 + C_H \times 0.013 \tag{4.6}$$

Finally, it is worth reminding that not only E_g plays a key role in the optical properties of a-Si:H, but α itself must exhibit high values. In our case, α above 4×10^4 cm^{-1} were achieved at 600 nm, this being a suitable value for the use of our material in solar cells.

4.3. Deposition conditions

The most important features of our state-of-the-art a-Si:H were presented in the previous section. Our results showed that not a clear set of deposition parameters could be given as a standard approach, as different sets of parameters lead to similar properties. As a result, comparison between conditions reported by different groups is not straightforward at all. Before summarizing the deposition conditions that led to high-quality a-Si:H, an evaluation of the role of the different parameters is indispensable to fully understand the process leading to our state-of-the-art layers.

4.3.1. Influence of filament temperature

The nature of the species released from the wire is strongly determined by T_f [Doyle et al. 1988, Gallagher 2001] and, as seen in *Chapter 3*, it drastically affects the microstructural features of thin silicon layers. In this section, the influence of T_f on the properties of a-Si:H will be presented. An inverted-basket shaped tantalum wire was used as in *Chapter 3*, whereas T_s = 200ºC, D_H = 0% and $P = 3.8\times10^{-2}$ mbar were selected. Regarding T_f, it was varied between 1500 and 1700ºC in this case. As a first result, the thickness (d) and the deposition rate (r_d) for samples under study are listed in Table 4.2.

T_f (ºC)	d (μm)	r_d (Å/s)
1500	0.70	3.9
1550	0.70	3.9
1600	0.75	4.2
1650	0.75	4.2
1700	0.80	4.4

Table 4.2. *Thickness and growth rate for a-Si:H samples as a function of T_f.*

The deposition rate did not change considerably over the whole range under study, as only a slight increase could be observed (from 3.9 to 4.4 Å/s) when T_f was raised from 1500 to 1700ºC. This result pointed out an efficient dissociation process, so that r_d seemed to be mainly limited by the silane supply and the geometric features of the deposition chamber.

FTIR spectra and the evolution of R^* are plotted in Fig. 4.14, where improved properties for samples deposited between 1600 and 1650ºC are observed ($R^* \sim 0.11$). This range led to the lowest Urbach front energies, though they remained relatively high ($E_u \sim 65$ meV at $T_f = 1650$ºC). E_u above 70 meV were obtained at lower T_f, whereas material with important crystalline fraction (leading to larger E_u values) was grown at $T_f \geq 1700$ºC.

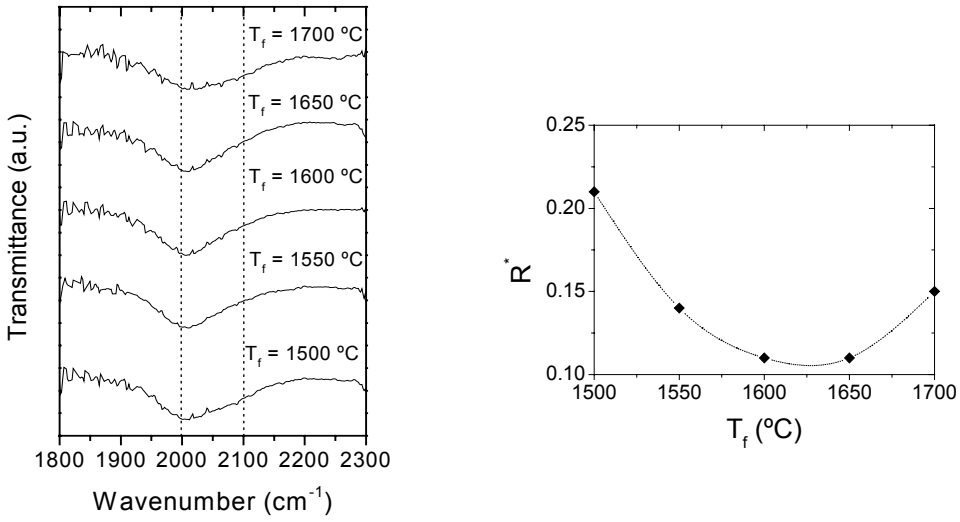

a) *b)*

Figure 4.14. *FTIR spectra (a) and R^* (b) as a function of T_f.*

Regarding electrical characterization, the evolution of σ_d and σ_{ph} for the amorphous samples in this series can be observed in Fig. 4.15(a), whereas *S* is shown in Fig. 4.15(b).

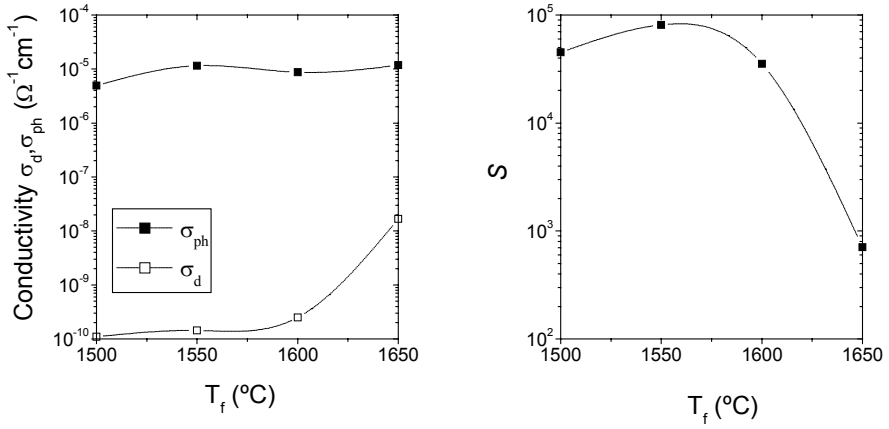

a) *b)*

Figure 4.15. *Electrical conductivities (σ_d and σ_{ph}) (a) and S of a-Si:H layers as a function of T_f (b)*

A remarkable increase in σ_d giving evidence of a clear worsening of the material properties was observed at $T_f > 1600$ºC, whereas σ_{ph} in the range of 10^{-5} $\Omega^{-1}cm^{-1}$ was obtained for all samples. Additionally, the evolution of *S* showed a maximum around $T_f = 1550$ºC. A slight shift between that range leading to improved microstructure (as determined by R^*) and the one resulting in enhanced electrical properties was observed. This result might be due to the presence of a certain crystalline phase, non-detectable by means of Raman spectroscopy, but capable of influencing the electronic features of the material.

In summary, the above-mentioned results showed that T_f determined the properties of a-Si:H, mainly through its influence on the H generation [Doyle et al. 1988, Molenbroek et al. 1996]. Nevertheless, the generation of atomic hydrogen at the filament does not depend uniquely on T_f, as the geometry of the filament itself plays also a very important role. An inverted-basket shaped filament with an area (A_f) of ~ 2.2 cm^2 was utilized in the present section, though a simple linear wire (A_f ~ 0.6 cm^2) was also employed in our laboratory. A shift of T_f towards higher temperatures was expected for the linear filament to achieve a similar H concentration. Effectively, higher T_f values (between 1650 – 1700ºC) were required for linear filaments to reach electrical properties comparable to those achieved with an inverted-basket shaped filament heated up to 1600ºC approximately.

4.3.2. Influence of pressure

The influence of *P* on the microstructural properties was already observed in *Chapter 3*. The observed behaviour was attributed to different growing precursors reaching the substrate. In that sense, it was mentioned that too high pressures led to crystallization due to enhanced production of atomic hydrogen. In this section, we will focus on the properties of purely amorphous samples deposited at different process pressure. *P* was varied between 5×10^{-4} and 9.2×10^{-2} mbar, so that the mean free path (λ_{mfp}) ranged between ~ 2 cm for $P = 5\times10^{-4}$ mbar and ~ 0.25 cm for 9.2×10^{-2} mbar as calculated from equation 3.3. The rest of the deposition conditions were kept constant (T_s = 200ºC, T_f = 1640ºC, ϕ_{SiH4} = 4 sccm, D_H = 0%) and an inverted-basket shaped tungsten filament was used. Amorphous samples deposited in this study are listed in Table 4.3, where both d and r_d are shown. Additionally, the $\lambda_{mfp}/d_{f\text{-}s}$ ratio has also been presented, as it plays a very important role as will be shown below.

P (mbar)	d (μm)	$\lambda_{mfp}/d_{f\text{-}s}$	r_d (Å/s)
5×10^{-4}	0.85	24.4	2.4
5×10^{-3}	1.0	9.8	3.7
1.0×10^{-2}	1.0	4.9	5.5
2.4×10^{-2}	2.7	2.0	7.5
3.8×10^{-2}	2.5	1.3	6.9
7.0×10^{-2}	2.0	0.7	5.6
9.2×10^{-2}	2.3	0.5	6.4

Table 4.3. *$d, \lambda_{mfp}/d_{f\text{-}s}$ and r_d for a-Si:H samples as a function of P. $d_{f\text{-}s}$ = 4 cm was used to calculate $\lambda_{mfp}/d_{f\text{-}s}$.*

Regarding the evolution of the structural features, not a clear trend could be observed by means of Raman spectroscopy (Fig. 4.16), as only a slight shift towards high wavenumbers could be guessed at intermediate pressures (2.4×10^{-2} – 3.8×10^{-2} mbar).

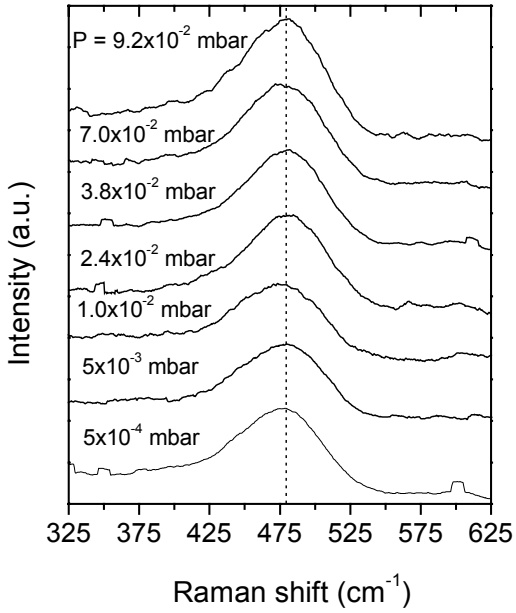

Figure 4.16. *Raman spectra as a function of P, where only a slight shift towards higher wavenumbers could be guessed at intermediate pressures.*

Nevertheless, clearer information could be obtained from FTIR measurements, which showed different degrees of microstructural order. In Fig. 4.17(a), the FTIR spectra in the region corresponding to the vibrational modes of hydrogen in both isolated (monohydride)

and non-isolated (multihydride or internal voids) configurations are shown. The evolution of the calculated R^* is also presented in Fig. 4.17(b).

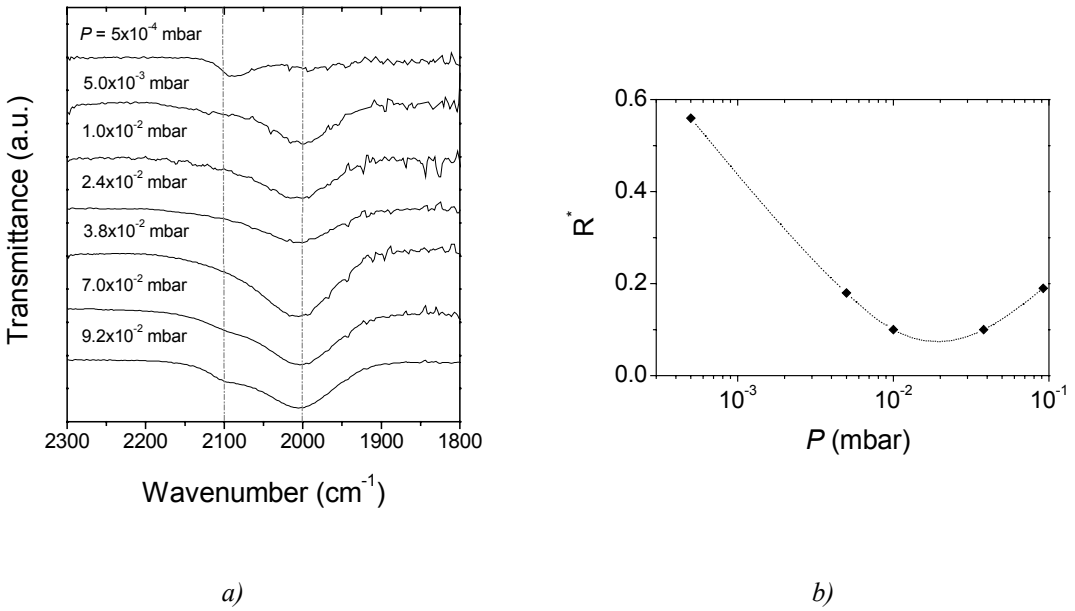

a) *b)*

Figure 4.17. *FTIR spectra (a) and R^* (b) indicating the different degree of order in a-Si:H as a function of P.*

As seen in Fig. 4.17(b), optimum ordering was obtained for P between 1×10^{-2} and 3.8×10^{-2} mbar, which yielded R^* values around 0.1. Similarly, the lowest E_u values as deduced from PDS data (~ 55 meV) were also obtained in that pressure regime as seen in Fig. 4.18. Conversely, high E_u values were obtained at either too high (E_u ~ 71 meV at P = 8.3×10^{-2} mbar) or too low pressures (E_u ~ 64 meV at $P = 5\times10^{-3}$ mbar).

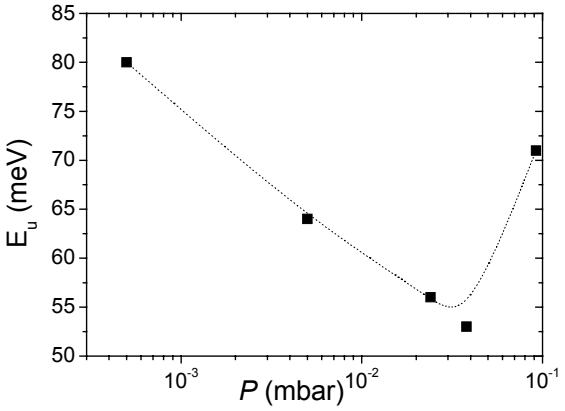

Figure 4.18. *E_u obtained from PDS measurements as a function of process pressure.*

Enhanced resistance to oxidation was also observed in samples deposited at intermediate *P* (Fig. 4.19), coherently with the low void density of the material. Samples deposited at too high (8.3×10^{-2} mbar) or too low pressures (5×10^{-4} mbar) exhibited an important absorption band around 1100 cm^{-1}, manifesting a significant presence of oxygen in the material.

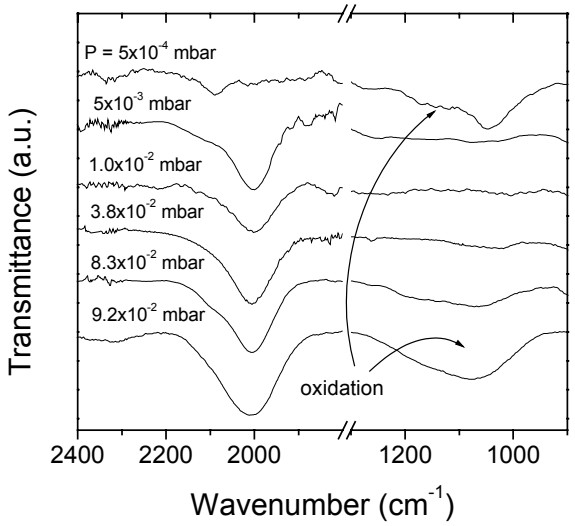

Figure 4.19. *Oxidation process as a function of deposition pressure manifesting different degree of compactness.*

Regarding electrical properties, the evolution of σ_d and σ_{ph} is shown in Fig. 4.20, where the improvement in material properties for samples deposited in the above-mentioned range can be also observed. σ_d reached its minimum value (around 10^{-10} $\Omega^{-1}cm^{-1}$) for samples deposited around 1.0×10^{-2} mbar indicating a sufficiently low defect density, whereas higher values were observed at both too low and too high pressures. E_A exhibited a similar trend, as E_A around 0.6 eV was obtained for that sample deposited at 5×10^{-4} mbar, indicating the probable presence of defects in the material. On the other hand, E_A values between 0.8 and 0.9 eV were achieved for the rest of the samples up to 1.1×10^{-1} mbar (not shown here), which led to the growth of nc-Si:H (see *Chapter 3*) and, consequently, to reduced E_A (around 0.6 eV). As far as σ_{ph} is concerned, it remained above 10^{-5} $\Omega^{-1}cm^{-1}$ for all samples. Clearer insight into the evolution of the electrical properties could be gained from the representation of *S*, whose maximum values were also obtained in the range from 1×10^{-2} to 3×10^{-2} mbar.

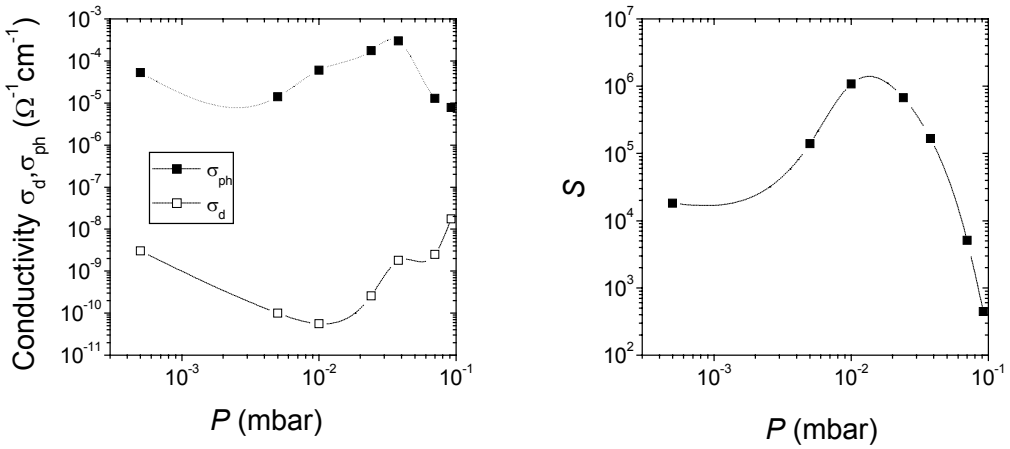

a) *b)*

Figure 4.20. *Electrical conductivities (σ_d and σ_{ph}) of a-Si:H as a function of pressure (a). The photoresponse (b) was determined from the values of σ_d and σ_{ph}.*

The behaviour observed can be explained by means of the influence of *P* on λ_{mfp}. The relation of λ_{mfp} and $d_{f\text{-}s}$ determines the transport regime (molecular or viscous) [Feenstra et al. 1999] and the number of secondary reactions, which determine the properties of the growth precursors [Papadopoulos et al. 1993, Molenbroek et al. 1997]. In that sense, the evolution of r_d can give some insight into the transport properties. A clear increase in r_d could be observed in the low-pressure regime (molecular transport) as *P* was varied between 5×10^{-4} mbar and 2.4×10^{-2} mbar (see Table 4.3). Conversely, r_d saturated or even decreased as *P* was further increased (λ_{mfp} comparable to $d_{f\text{-}s}$), which led to viscous transport.

Regarding secondary reactions, too low pressures (below 1.0×10^{-2} mbar) led to very large λ_{mfp}, so that an important amount of the species generated at the filament reached the growing surface without undergoing secondary reactions. This trend led to porous structures, as the growth precursors generated at the filament (mainly atomic silicon, Si) are characterized by their high sticking coefficient. On the other hand, too high pressures (between 5.0×10^{-2} and 9.2×10^{-2} mbar) led to very low values of λ_{mfp}, which seemed to induce an excessive number of secondary reactions resulting in higher silanes, which are also characterized by their low surface mobility. Once more, a disordered and porous structure with very low optoelectronic properties was grown. Finally, *P* yielding high-

quality layers gave rise to λ_{mfp} values between 4.5 cm and 1.5 cm approximately, which resulted in $\lambda_{mfp}/d_{f\text{-}s}$ ratios between 1.1 and 0.4 ($d_{f\text{-}s}$ was 4 cm in our experimental set-up). The importance of *P* and the relationship between λ_{mfp} and $d_{f\text{-}s}$ can be quantified by means of a new parameter: $P{\cdot}d_{f\text{-}s}$ [Molenbroek et al. 1997], which serves as an indicator of the number of gas-phase reactions. This parameter presented an optimum range of 4 - 12($\times 10^{-2}$) Pa(mbar)·cm in our experiments, which was consistent with reported values [Molenbroek et al. 1997, Feenstra et al. 1999]. From the observed behaviour, it could be deduced that a decrease in $d_{f\text{-}s}$ could be compensated by an increase in *P* and vice versa, thus keeping the number of secondary reactions approximately constant.

4.3.3. Influence of hydrogen dilution

The beneficial role of hydrogen dilution in a-Si:H deposited by PECVD was already demonstrated in 1981 [Guha et al 1981]. Similarly, moderate D_H (lower than in PECVD) led also to improved properties in Hot-Wire CVD [Feenstra et al. 1999], especially when dealing with stability issues [Bauer et al. 1998b] and low T_s [Alpuim et al. 1999]. In the latter case, the additional production of atomic hydrogen seemed to favour the surface mobility of species, thus compensating for the low T_s. Regarding our studies, D_H was observed to determine the crystallinity of deposited samples (*Chapter 3*). Similar deposition conditions to those seen in *Chapter 3* were also employed in this study: T_s = 200ºC, T_f = 1640ºC, $P = 3.8\times10^{-2}$ mbar and inverted-basket shaped tungsten filament. As far as D_H itself is concerned, this parameter was varied between 0 and 75% by keeping ϕ_{SiH4} fixed at 4 sccm and ϕ_{H2} ranging from 0 to 12 sccm. First of all, both d and r_d for samples under study are listed in Table 4.4.

D_H (%)	d (μm)	r_d (Å/s)
0	*1.10*	*4.1*
25	*0.85*	*5.7*
50	*0.90*	*3.3*
75	*0.80*	*4.4*

Table 4.4. *d and r_d for a-Si:H samples considered in the D_H study*

Raman spectra gave evidence the transition from a-Si:H to nc-Si:H at D_H ~ 75% (Fig. 4.21). Anyhow, it was difficult to extract any information from this measurements as far as a-Si:H layers were concerned.

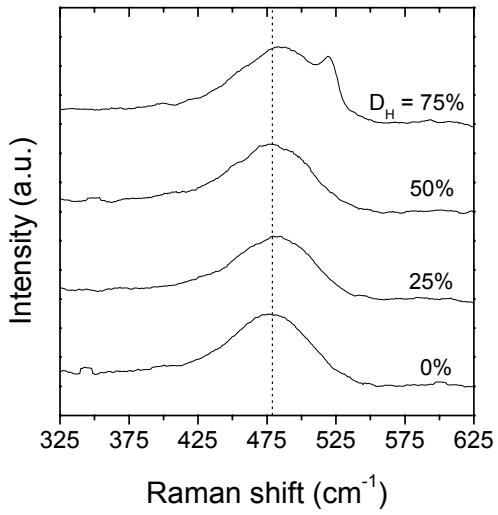

Figure 4.21. *Raman spectra for samples deposited at different D_H values. A mixture between amorphous and crystalline phase can be observed at D_H = 75%.*

Regarding FTIR measurements, the evolution of R^* is presented in Fig. 4.22. In this case, improved structural features could be achieved at moderate hydrogen dilutions (R^* decreased from 0.12 to 0.09 as D_H was varied from 0 to 25%).

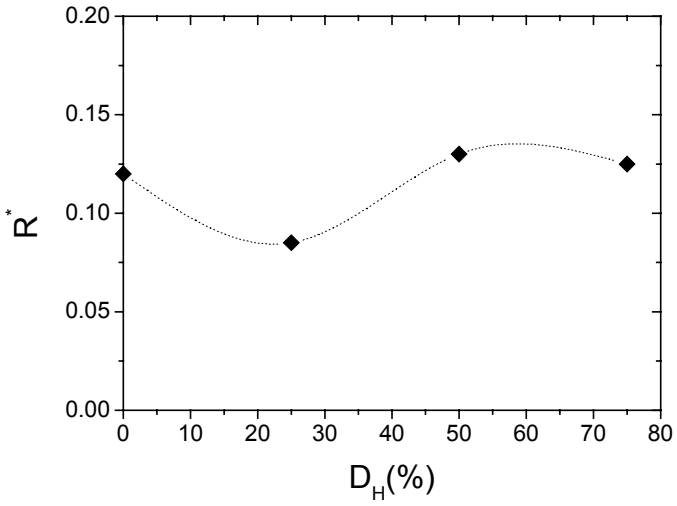

Figure 4.22. *R^* indicating the different degree of order in a-Si:H as a function of D_H.*

A similar trend was also observed when considering the electrical properties. In Fig. 4.23, the electrical conductivity (both σ_d and σ_{ph}) and $\mu\tau$ are presented.

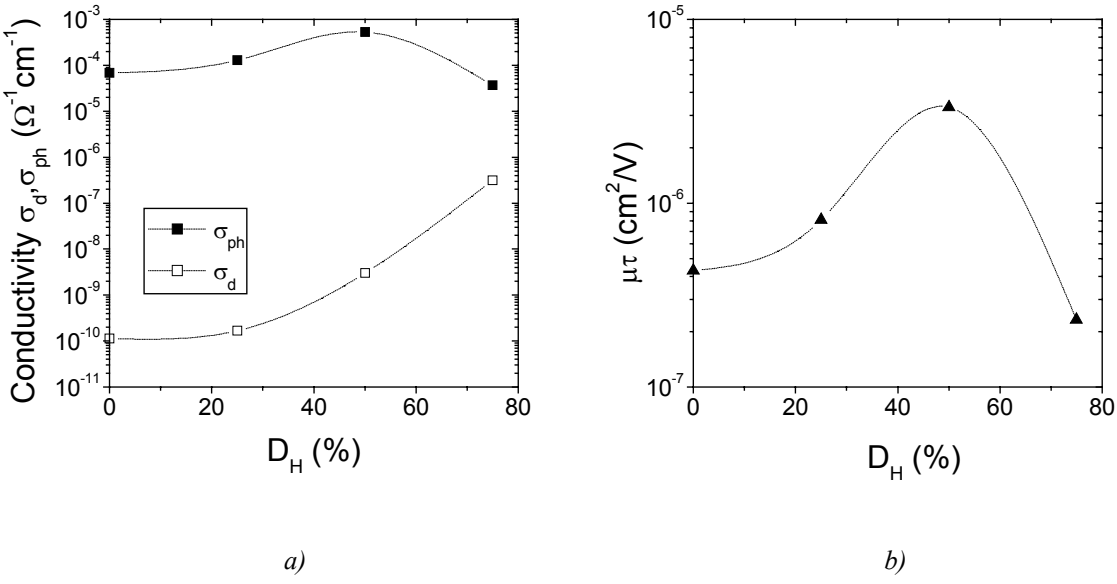

a) *b)*

Figure 4.23. *Electrical conductivities (σ_d and σ_{ph}) of a-Si:H (a) and $\mu\tau$ (b) as a function of D_H.*

σ_d and σ_{ph} values around 10^{-10} $\Omega^{-1}cm^{-1}$ and 10^{-4} $\Omega^{-1}cm^{-1}$ respectively were measured for layers deposited at low D_H ($\leq$ 25%) and only a slight increase in σ_{ph} could be seen for that sample obtained at D_H = 25%. A similar result could also be observed for $\mu\tau$, which also increased after moderate dilutions. Regarding samples deposited at $D_H \geq$ 50%, a different behaviour was observed. Thus, remarkably higher σ_{ph} (and $\mu\tau$) could be achieved at D_H = 50%, although too large σ_d values manifested the presence of electronically active impurities. Finally, that sample deposited at D_H = 75% exhibited poor properties as, in fact, the material consisted of a mixture of both amorphous and crystalline phases as can be seen in Fig. 4.21. On the other hand, E_A values around 0.85 eV were obtained for all samples deposited at D_H lower than 50%, whereas E_A = 0.61 eV was measured at D_H = 75% indicating the presence of an important crystalline fraction. Additional insight into the electrical properties is given by *S*, whose evolution has been presented in Fig. 4.24. A very subtle improvement could be observed at moderate dilutions ($D_H \leq$ 25%), whereas a clear worsening was observed at higher dilutions. Nevertheless, the improvement observed after moderate dilution was not very remarkable, this being an indication of efficient production of atomic hydrogen, even when using pure silane as reactant gas.

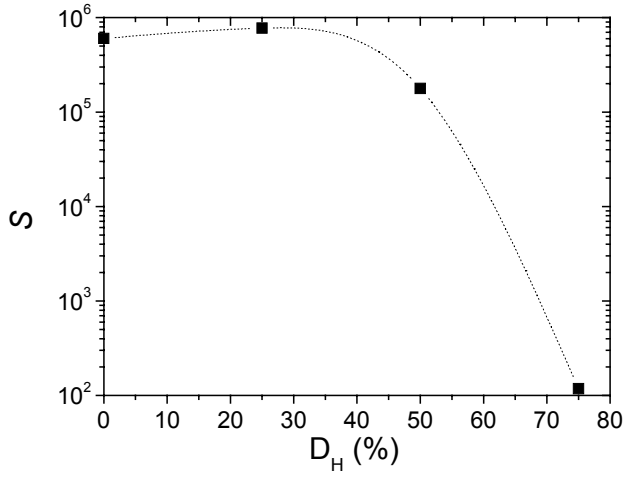

Figure 4.24. *S as a function of D_H showing slightly increased values at moderate D_H.*

In summary, the behaviour observed in this section pointed to the beneficial role of moderate hydrogen dilution, although no drastic changes were observed in accordance with reported results [Bauer et al. 1998b, Feenstra et al. 1999]. Moderate dilutions led to enhanced production of atomic hydrogen at the surface of the filament, so that the concentration of atomic hydrogen near the substrate was also favoured, which seemed to contribute to the deposition of highly ordered material. On the other hand, high D_H ($\geq 50\%$) values seemed to lead to the growth of highly porous material with unsuitable properties and, eventually, to the growth of thin silicon layers exhibiting an important crystalline fraction.

4.4. Summary

The role of the different technological parameters on the material properties was evaluated, so that our state-of-the-art material was characterized. Intrinsic a-Si:H layers exhibiting compact and ordered structure ($R^* \sim 0.11$, $E_u \sim 55$ meV) and suitable electrical features ($\sigma_d \sim 1\times10^{-10}$ $\Omega^{-1}cm^{-1}$, $\sigma_{ph} \sim 5\times10^5$ $\Omega^{-1}cm^{-1}$, $L_D > 200$ nm) were obtained. On the other hand, typical E_g values around 1.7 eV were measured for our optimized material. Finally, slightly high density of defects ($N_d \sim 5\times10^{16}$ cm^{-3}) was measured, this result being probably related to the low substrate temperature used throughout our work. Regrettably, the dependence on geometrical issues and the correlation between parameters did not allow

to clearly define a unique set of optimised conditions. Nevertheless, different conclusions could be extracted and are next mentioned.

1) The concentration of atomic hydrogen strongly determined the material properties. In that sense, breakage of weak Si-Si bonds, formation of Si-H bonds, H diffusion into the film and enhanced mobility of the radicals resulted in a relaxed structure. Furthermore, filament characteristics clearly affected the atomic hydrogen production. In our case, T_f between 1550 and 1650ºC was used for inverted basket shaped filaments ($A_f \sim 2.2$ cm^2) whereas higher T_f were required when using linear wires ($A_f \sim 0.6$ cm^2). Although no systematic studies have been performed yet in our laboratory, the use of small area filaments and high filament temperatures might result in longer lifetimes of the filaments, as silicide formation is minimized for high T_f values. In that sense, and from a technological point of view, the use of low area filaments and high T_f seems to be the preferable situation.

2) P and $d_{f\text{-}s}$ were clearly related, so that $P \cdot d_{f\text{-}s} \sim 4 - 12(\times 10^{-2})$ Pa(mbar)·cm was required in our case to obtain device-quality a-Si:H. These values allowed the atomic silicon produced at the surface of the filament to be consumed before reaching the substrate, giving place to high mobility species. On the other hand, this $P \cdot d_{f\text{-}s}$ range did not lead to an excessive number of secondary reactions, which would have given rise to the formation of low mobility higher silanes. In our case, $d_{f\text{-}s}$ ranged between 3 and 5 cm for the inverted basket filament geometry and 4 cm for the linear ones. These values led to optimum working pressures between 1.0×10^{-2} and 3.0×10^{-2} mbar.

3) As H played a dramatic role, hydrogen dilution was also observed to strongly affect the properties of the material. In that sense, the production of H in our reactor seemed to be an efficient process, so that only a subtle improvement could be observed at moderate hydrogen dilutions ($D_H \leq 25\%$). Conversely, larger hydrogen dilutions led to unsuitable material properties or to layers exhibiting significant crystalline fractions ($D_H \geq 75\%$).

5. Hot-Wire deposited doped material

In this chapter we study the optical and electrical properties of both n- and p-type thin silicon films. In particular, special attention is paid to the deposition of p-type layers due to the specific difficulties associated to their production. In that sense, both p-type a-Si:H and nc-Si:H samples are analysed and special treatments to improve their properties described. Finally, the photovoltaic suitability of the deposited layers is examined.

5.1. Introduction

The capability to grow both p- and n-type doped material with suitable properties is a key issue in the fabrication of amorphous thin film silicon photovoltaic devices. Thus, the *built-in* voltage (V_{bi}) of solar cells (and consequently their open circuit voltage, V_{oc}) depends dramatically on the position of the Fermi level of the p- and n-type layers at both sides of the device. As the doping efficiency increases, V_{bi} shifts to higher values, thus enhancing the performance of the solar cell. Moreover, suitable electrical properties are required to prevent parasitic effects at the junctions between the doped layer and, either the TCO at the front contact or the metal at the rear one. Otherwise, not-ohmic behaviours and/or increased series resistances are observed, which dramatically degrade the solar cell.

Doping of a-Si:H was first demonstrated by Spear and LeComber [Spear and LeComber 1975], who showed the capability to obtain both p- and n-type material by PECVD. Suitable amounts of either diborane (B_2H_6) for p-type material or phosphine (PH_3) for n-type layers were added to the gas mixture in the reactor. This result demonstrated the enormous potential of a-Si:H, thus overcoming one of the first limitations associated to a-Si:H. Hence, the disordered structure of a-Si:H was supposed to allow the incorporation of dopant atoms in their most favourable coordination number into the amorphous network, thus impeding the doping of the material. Later on, the doping mechanism of a-Si:H was further clarified by Street [Street 1991].

Hot-Wire CVD has shown its capability to produce intrinsic a-Si:H with properties as satisfactory or, even better, than those obtained by means of PECVD [Matsumura 1986,

Mahan et al. 1991]. Nevertheless, few studies have been published regarding the doping of a-Si:H or nc-Si:H deposited by Hot-Wire CVD [Brogueira et al. 1997, Voz et al. 2000b, Alpuim et al. 2001, Conde et al. 2001, Fonrodona et al. 2001]. Moreover, it is not unusual to use heavily doped contact layers produced by PECVD, even when dealing with devices incorporating intrinsic layers grown by Hot-Wire CVD [Nelson et al. 1994, Bauer et al. 1998, Conde et al. 2001, Klein et al. 2001, Van Veen and Schropp 2002, Ide et al. 2003]. Anyhow, it is obvious that some drawbacks arise from the combination of two different techniques, especially when dealing with later industrial applications. Thus, a trend to grow doped layers by Hot-Wire CVD has gained attention and results have been reported on a-Si:H based devices entirely deposited by this technique [Wang et al. 2000, Weber et al. 2000, Mukherjee et al. 2001, Nelson et al. 2001, Mahan et al. 2002, Kupich et al. 2003].

In the following sections, our results concerning the deposition of both n- and p-type layers will be described. Special attention will be paid to the p-type material, as its production is known to be especially problematic.

5.2. n-type material

n-type samples were obtained by adding PH_3 to the gas mixture. The deposition conditions used in this study were similar to those leading to our high-quality intrinsic a-Si:H as seen in *Chapter 4*. Intermediate pressures between 1.0×10^{-2} and 3.0×10^{-2} mbar were employed in order to allow the production of high-mobility species through secondary reactions. On the other hand, substrate temperature (T_s) around 200ºC and T_f = 1650ºC were used. Moreover, no hydrogen dilution was used, as it only provoked a slight improvement in intrinsic layers. Finally, a [P]/[Si] ratio of 1% was selected, where [P]/[Si] refers to the atomic ratio in gas phase, which might differ from the solid phase ratio measured in the grown sample. The deposition conditions have been summarized in Table 5.1.

T_s (ºC)	T_f (ºC)	P (mbar)	ϕ_{SiH4} (sccm)	D_H (%)	[P]/[Si] (%)
200	1650	1.0×10^{-2} - 3.0×10^{-2}	4	0	1.0

Table 5.1. *Deposition conditions for n-type doped a-Si:H. [P]/[Si] refers to the atomic relation in gas phase.*

A linear Ta filament was used for samples presented in this section resulting in deposition rates (r_d) around 6 Å/s. As far as structural characterization is concerned, both FTIR spectroscopy and Raman results are plotted in Fig. 5.1 for our state-of-the-art n-type material.

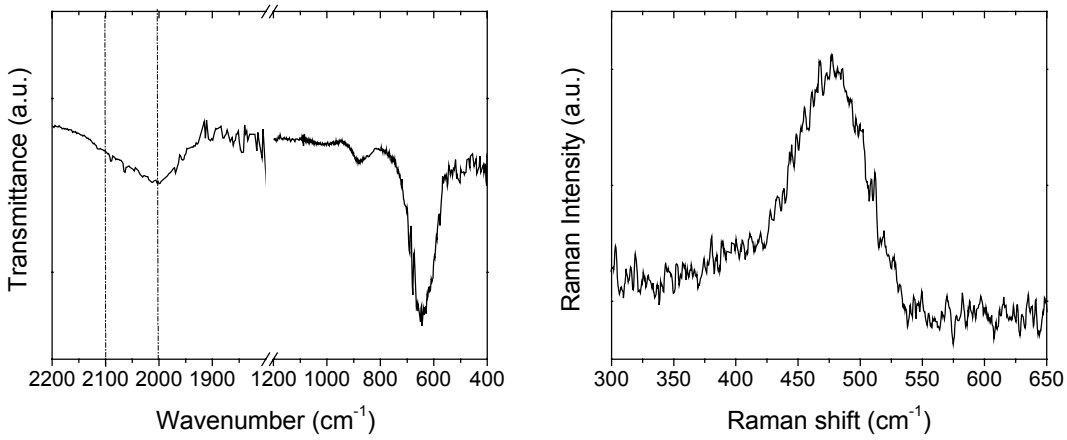

a) *b)*

Figure 5.1. *FTIR (a) and Raman (b) spectra showing the structural properties of n-type a-Si:H.*

A dense structure was evidenced by FTIR spectroscopy measurements, as no contribution around 1100 cm^{-1} corresponding to oxygen incorporation could be observed. Nevertheless, microstructure factors (R^*) around 0.2-0.25 were obtained, this being a higher value than the one observed in intrinsic a-Si:H grown at similar conditions. In fact, a worsening of the structural properties after the incorporation of dopant atoms into the amorphous network is an expected result [Brogueira et al. 1997]. Regarding the total amount of hydrogen, a high C_H value around 17% was observed, in accordance with the high value of R^*, both pointing to an excessive presence of hydrogen not bonded in the monohydride configuration. On the other hand, the amorphous structure of the material was attested by Raman spectroscopy. Thus, a broad peak was observed at 480 cm^{-1}, whereas not a trace of the peak at 520 cm^{-1} corresponding to the crystalline fraction could be detected.

Regarding optical characterization, a typical Photothermal Deflection Spectroscopy spectrum for our n-type material can be observed in Fig. 5.2. Besides, Table 5.2 presents the values of the optical band gap (E_g), the Urbach front energy (E_u), and the midgap density of states (N_d), as deduced from the shown PDS spectrum.

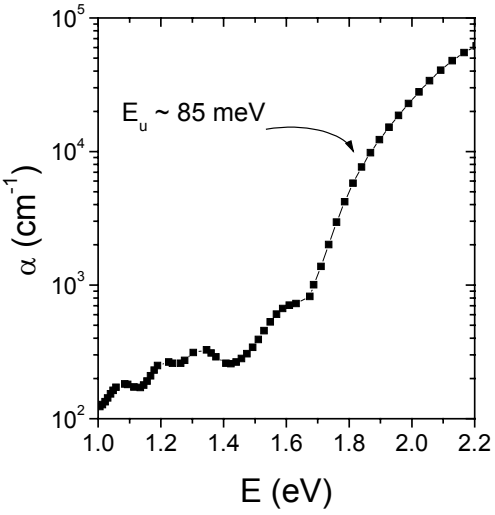

Figure 5.2. *Absorption spectrum obtained by PDS for an n-type a-Si:H sample.*

E_g (eV)	E_u (meV)	N_d (cm^{-3})
1.7	85	1.5×10^{18}

Table 5.2. *E_g, E_u and N_d for n-type a-Si:H.*

As seen in Table 5.2, a typical a-Si:H value was obtained for E_g, whereas larger E_u and N_d were observed. This result was coherent with the enhanced disorder, which was already demonstrated by FTIR spectroscopy. The high value of N_d pointed to a high concentration of midgap defect states, which limit the transport properties of the material. Nevertheless, this result was not as critical as it was for the active layer, where carrier collection takes place. It is worth reminding that the most important function of doped layers is to give rise to the *built-in* voltage and provide good electrical contact with the electrodes, whereas not a significant contribution to carrier collection is attributed to them.

Finally, electrical properties are presented in Fig. 5.3, where the Arrhenius plot of the conductivity as a function of temperature for our state-of-the-art n-type material is shown. The value of the room temperature conductivity (σ_d) was ~ 1.4×10^{-2} Ω^{-1}cm^{-1}. This value was similar to that of PECVD samples obtained at similar phosphine gas-phase concentrations [Street 1991]. Moreover, similar results for comparable deposition conditions have been reported [Brogueira et al. 1997, Alpuim et al. 2001]. Activation

energies (E_A) around 0.25 eV were obtained, this value being also comparable to those reported for PECVD material. In summary, electrical requirements for the implementation of n-type layers in photovoltaic devices, namely, σ_d values above 10^{-3} $\Omega^{-1}cm^{-1}$and E_A below 0.3 eV [Schropp and Zeman 1998], were fulfilled by our state-of-the-art material.

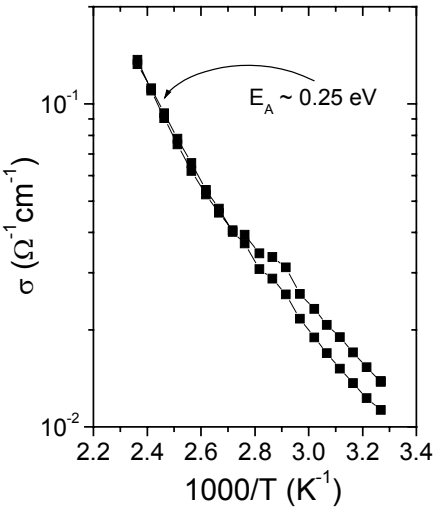

Figure 5.3. *Arrhenius plot corresponding to n-type a-Si:H material.*

5.3. p-type material

p-type doping of silicon thin films is usually achieved by adding a boron containing gas into the deposition chamber. Diborane (B_2H_6) is the most widely employed dopant gas, although some difficulties arise from its use due to its thermal instability [Collins 1988, Roca i Cabarrocas et al. 1989]. Alternative gases, such as trimethylboron ($B(CH_3)_3$, TMB) have also led to p-type layers with suitable properties [Brogueira et al. 1997, Jadkar et al. 2000] without undergoing thermal instability.

Electrical properties are, obviously, of critical importance when evaluating the suitability of p-type material. High conductivity is required to obtain acceptable V_{bi} and to ensure proper contact properties at both the p/i and the p/TCO interfaces. Nevertheless, not only electrical properties must be taken into account, as also optical features do play a key role in this case. The illumination of solar cells is commonly performed through the p-type layer, so the collection of holes, whose transport properties are clearly worse than those of

electrons, is enhanced [Guha et al. 1986, Chatterjee et al. 1998]. Consequently, low optical absorption over the short wavelength region of the visible spectrum is required for the p-type layer. Different materials have been proposed as an alternative to p-type a-Si:H, namely, boron doped carbonised amorphous silicon (a-SiC:H:B), due to its high band gap above 2 eV [Merten 1996], boron doped microcrystalline fluorinated silicon (μc-Si:H:F:B), combining both high band gap and low absorption coefficient (α) due to its indirect gap [Guha et al. 1986], or boron doped microcrystalline (or nanocrystalline) silicon (μc-Si:H or nc-Si:H) [Wanka et al. 1995, Rath and Schropp 1998, Mukherjee et al. 2001, Miyajima et al. 2003]. In this section, results concerning p-type a-Si:H and nc-Si:H are presented, while the incorporation of these materials both solely and combined in solar cells is described in *Chapter 6*.

p-type doping of a-Si:H by Hot-Wire CVD is not a straightforward process [Alpuim et al. 2001], making it difficult to obtain σ_d values comparable to those reported in PECVD samples. Moderately high substrate temperature [Brogueira et al. 1997] or post-annealing treatments [Alpuim et al. 2001], which have also shown its potential in PECVD [Roca i Cabarrocas 1994], have been proposed as different strategies to overcome that difficulty. Our best results concerning p-type a-Si:H will be presented next, whereas, later on, results on p-type nc-Si:H will be also analysed.

5.3.1. p-type a-Si:H

p-type a-Si:H at our laboratory was mainly obtained by the addition of B_2H_6 to the gas mixture. Some experiments were also performed with TMB, although not a clear correlation with the dopant gas used could be deduced from our studies.

A first step was made where similar conditions to those leading to our state-of-the-art intrinsic a-Si:H were used. Nevertheless, T_s was lowered to 125ºC to prevent damaging effects arising from the well-known thermal instability of B_2H_6 [Collins 1988, Roca i Cabarrocas et al. 1989, Peiró et al. 1998, Voz et al. 2000b]. Besides, a [B]/[Si] ratio of 1% in gas phase was used as seen in Table 5.3 (sample *AP1*). Subsequently, higher substrate temperature (*AP2*) and increased dopant concentration up to 10% (*AP3*) were studied.

Sample	T_s (ºC)	T_f (ºC)	P (mbar)	ϕ_{SiH4} (sccm)	D_H (%)	[B]/[Si] (%)
AP1	125	1640	3.8×10^{-2}	4	0*	1.0
AP2	450	1900	1.2×10^{-2}	10	0*	1.0
AP3	125	1850	1.0×10^{-2}	4	0*	10.0
AP4	125	1850	1.0×10^{-2}	4	0*	5.0

Table 5.3. *Deposition conditions for p-type doped a-Si:H. [B]/[Si] refers to the atomic ratio in gas phase. *B_2H_6 was highly diluted (95%) in hydrogen. r_d values around 8 Å/s were measured for all samples.*

Similar structural properties to those observed in n-type a-Si:H were obtained in sample *AP1*. Thus, no significant oxidation was observed after FTIR spectroscopy measurements, whereas R^* values around 0.22 were measured as seen in Fig. 5.4(a). Regarding Raman spectra, only the broad contribution around 480 cm^{-1} was observable (Fig. 5.4(b)), giving evidence of the amorphous character of the samples.

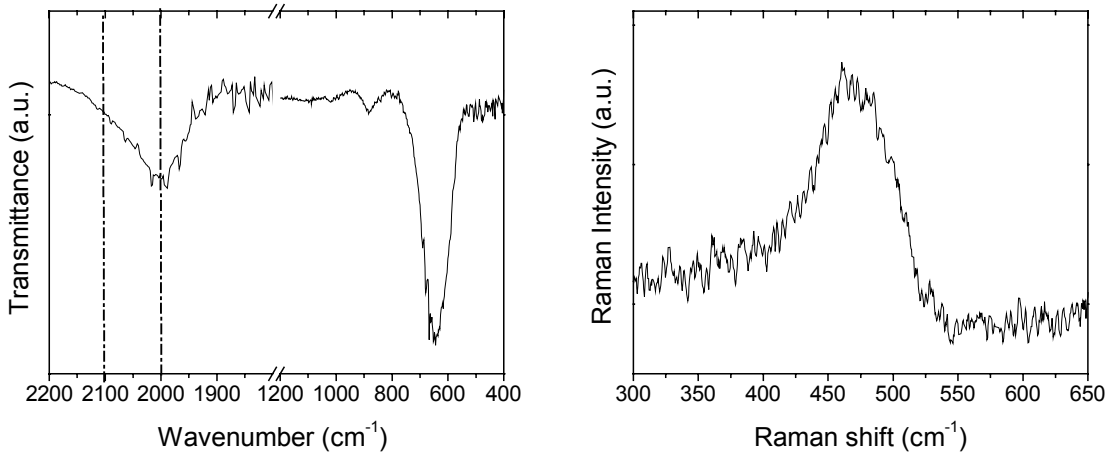

a) *b)*

Figure 5.4. *Structural properties of sample AP1. FTIR (a) and Raman (b) spectra are represented.*

As far as PDS measurements are concerned (Fig. 5.5), high E_u and N_d values ($E_u \sim 95$ meV and $N_d \sim 8\times10^{17}$ cm^{-3}) evidenced a more disordered structure than in intrinsic a-Si:H deposited at similar conditions. This result was in fact expected and can be attributed to the incorporation of boron atoms into the amorphous network, similarly to the result observed after P atoms incorporation in n-type layers.

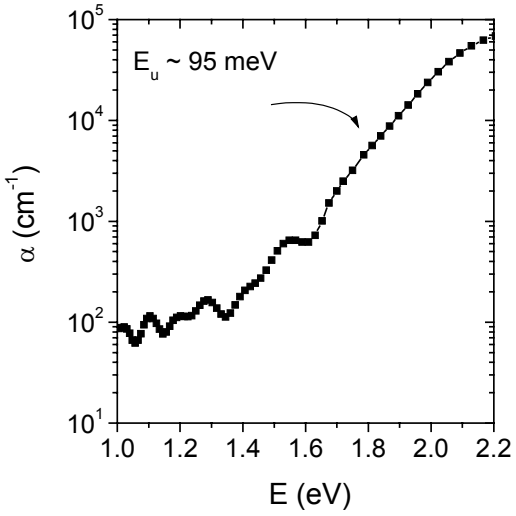

Figure 5.5. *Optical absorption spectrum obtained by PDS for sample AP1.*

Finally, σ_d around 1×10^{-6} $\Omega^{-1}cm^{-1}$ and E_A ~ 0.56 eV were measured for sample *AP1* from the σ Arrhenius plot (Fig. 5.6). These values were poorer than those achieved in PECVD samples, where σ_d above 1×10^{-5} $\Omega^{-1}cm^{-1}$ and E_A below 0.5 eV are obtained [Street 1991].

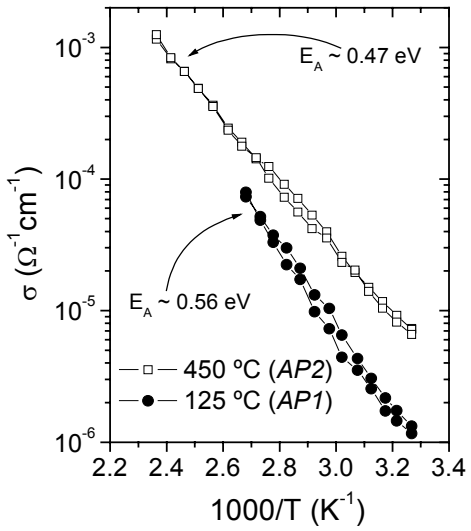

Figure 5.6. *Arrhenius plot of p-type a-Si:H material deposited at either 125ºC (●) or 450ºC (□).*

Poorer structural properties, which might be solved after conveniently varying the deposition conditions, may have accounted for the unsuitable electrical features of our Hot-Wire CVD p-type material. Besides, either lower solid-phase incorporation of dopant

atoms, or different dopant activation leading to worse electrical properties even when dealing with similar boron concentrations in the material, might also have been responsible for the observed result.

From the previous observations and, as a first step to improve our p-type a-Si:H, high substrate temperature (T_s = 450ºC) and deposition conditions leading to a more ordered structure were tested (sample *AP2*). This layer exhibited higher conductivity, $\sigma_d \sim 8\times10^{-6}\ \Omega^{-1}cm^{-1}$, and lower activation energy, $E_A \sim 0.47$ eV, than those achieved in *AP1* material. These values were closer to those obtained by PECVD and showed that the poor electrical behaviour observed at low-substrate temperatures (*AP1*) might be, at least partially, improved after variation of the growth conditions. The dark conductivity Arrhenius plot of sample *AP2* has been also represented in Fig. 5.6, so that the difference between both materials can be clearly seen. The improved features of p-type a-Si:H after an increase in T_s might seem surprising, as this fact apparently contradicts the well-known harmful effect of B_2H_6 thermal decomposition. The reason behind this improvement could be an increasing in the dopant activation associated to enhanced structural order of the material and lower hydrogen content.

In order to get more information on the doping process, sample *AP1* was annealed at increasing temperatures. Annealing temperatures (T_{ann}) of 200, 300 and 375ºC were selected and an annealing time of 1 hour was chosen. Moreover, the experiment was carried out at a pressure around 10^{-5} mbar to prevent oxidation. The Arrhenius plot of the dark conductivity for every annealing temperature has been presented in Fig. 5.7, where a dramatic improvement in both σ_d and E_A can be observed at increasing temperatures. Only a slight improvement could be observed after a 1-hour annealing at 200ºC, which gave rise to $\sigma_d \sim 3\times10^{-6}\ \Omega^{-1}cm^{-1}$ and $E_A \sim 0.51$ eV. A clearer influence was observed at 300ºC ($\sigma_d \sim 2\times10^{-5}\ \Omega^{-1}cm^{-1}$ and $E_A \sim 0.50$ eV) and, eventually, $\sigma_d \sim 1\times10^{-4}\ \Omega^{-1}cm^{-1}$ and $E_A \sim 0.41$ eV were achieved at T_{ann} = 375ºC, these values being comparable to those typically reported for PECVD-obtained samples.

The behaviour observed after subsequent annealing processes can be attributed to the activation of boron atoms, which are known to form boron-hydrogen complexes at low substrate temperatures [Pankove et al. 1985, Alpuim et al. 2001] as those used in *AP1*

sample. This material exhibited high hydrogen content (C_H ~ 16%) as measured by FTIR spectroscopy, so the formation of these complexes was favoured. Boron atoms forming these complexes are neutralized by atomic hydrogen and do not effectively contribute to the doping of the material, as they bond with their optimal valency (three-fold coordination). Nevertheless, B-H bonds can be broken by annealing at sufficiently high temperatures above the equilibrium temperature. The resulting boron atoms might then be incorporated into the amorphous matrix adopting the four-fold configuration and thus contributing to the substitutional doping of the material.

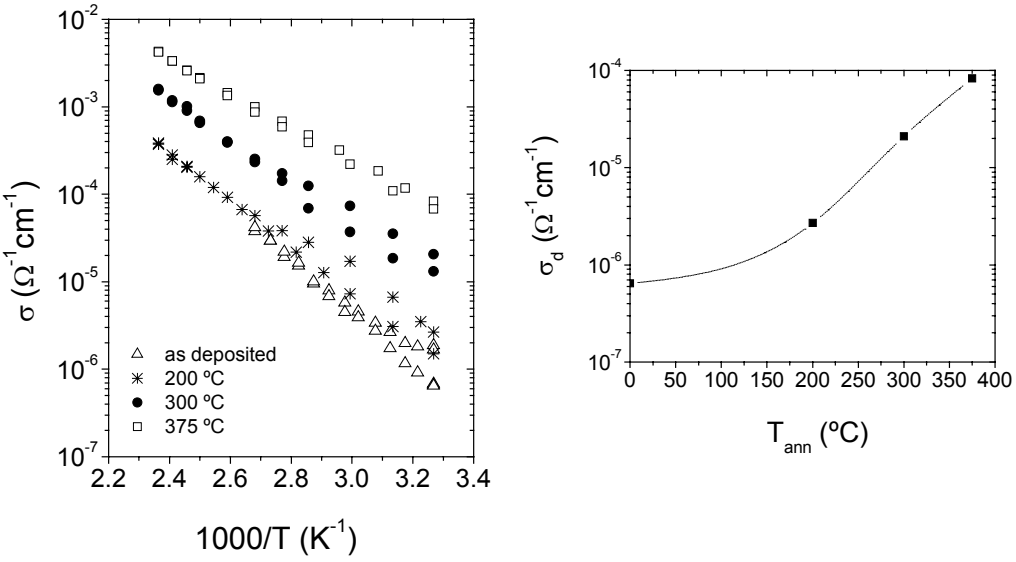

a) *b)*

Figure 5.7. *Arrhenius plots of sample AP1 in the as-deposited state (△) and after subsequent annealings at 200ºC (∗), 300ºC (●) and 375ºC (□) (a). Evolution of σ_d as a function of T_{ann} (b).*

In order to get a deeper understanding on the annealing process, a mass analyser was used to monitor the hydrogen effusion during the heating of the samples. Detailed studies have been reported regarding the role of hydrogen effusion. In particular, the influence of doping on H evolution was described by [Beyer 2003]. In Fig. 5.8, the evolution of hydrogen after annealing for an *AP1* sample has been plotted to intuitively understand the important role of hydrogen effusion. H_2 could be detected for temperatures above 240ºC approximately, thus giving rise to a first effusion peak around 270ºC. This is pointed as the probable beginning of the doping activation process. Further increase of the annealing temperature led to different effusion contributions at temperatures around 390, 440 and

470ºC. Nevertheless, the annealing temperature was kept below 375ºC in most of our experiments, so only those peaks at 270 and 390ºC were expected to clearly affect the activation mechanism in our samples.

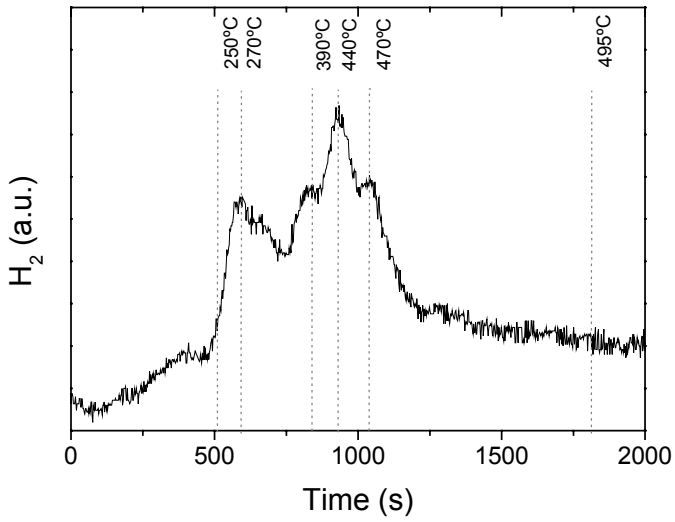

Figure 5.8. *Hydrogen effusion during heating of an AP1-type sample.*

Finally, and in order to avoid the high temperature steps involved in both the high T_s deposition and the annealing process, a different approach was considered. In this case, a larger amount of boron was introduced into the reactor chamber, so that a sufficient amount of boron atoms was expected to contribute to the doping mechanism. A [B]/[Si] ratio of 10% was used and the sample was labelled as *AP3*. Moreover, T_f was increased up to 1850ºC to prevent deleterious effects associated to the absorption of boron atoms by the filament. In sample *AP3*, a much larger amount of boron than in *AP1* layers is introduced into the reactor, so this effect might have been especially critical. Figure 5.9 shows the Arrhenius plots of σ for samples obtained using different boron concentrations. A dramatic improvement was obtained after conveniently increasing the dopant concentration, so that σ_d around 6×10^{-5} $\Omega^{-1}cm^{-1}$ and E_A = 0.45 eV were obtained for sample *AP3* showing the good electrical properties of this material and indicating that a sufficient number of boron atoms did effectively act as doping atoms.

Regarding the structural properties of the material, an increased disorder could be observed for sample *AP3* due to the increased incorporation of boron. Thus, PDS spectra for sample

AP3 and another layer deposited under the same deposition conditions but with a [B]/[Si] ratio of 5% (labelled *AP4*) are shown in Fig. 5.10(a).

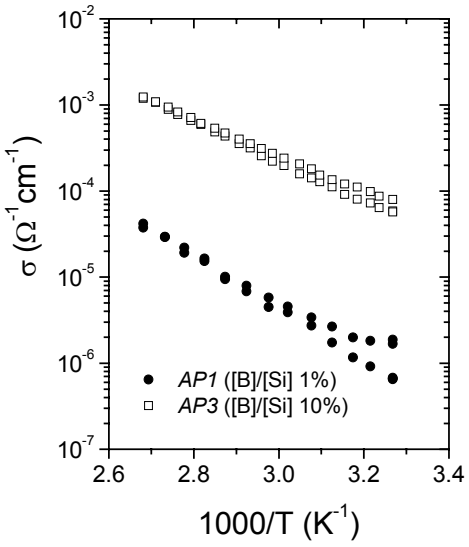

Figure 5.9. *Arrhenius plots of samples obtained at [B]/[Si] = 1% (AP1) and 10% (AP3).*

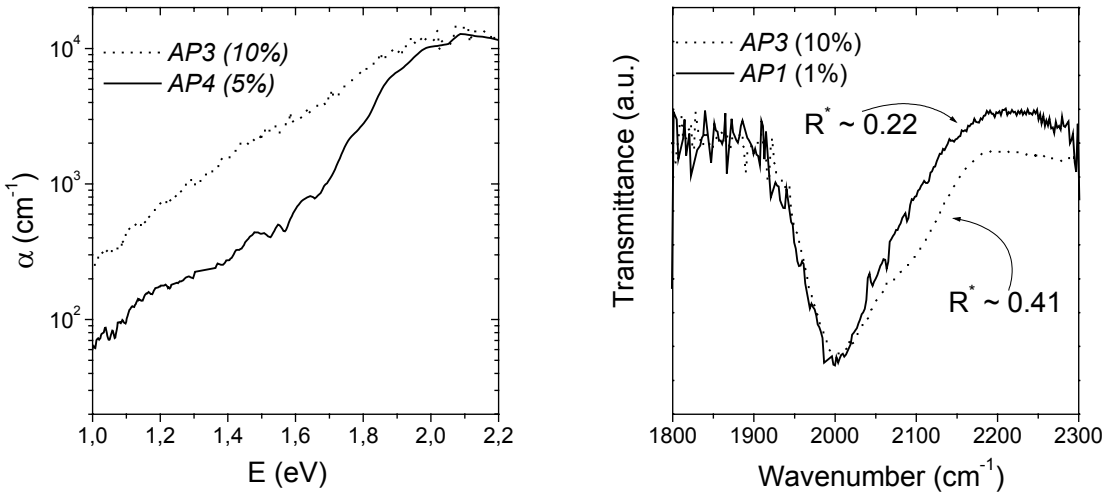

a) *b)*

Figure 5.10. *PDS (a) and FTIR (b) spectra for p-type a-Si:H exhibiting different [B]/[Si] ratios. Sample AP1 was obtained at [B]/[Si] = 1%, whereas 10% and 5% where used for layers AP3 and AP4 respectively.*

Similarly, FTIR spectra for samples *AP1*(1%) and *AP3*(10%) and the corresponding microstructure factors are shown in Fig. 5.10(b), where R^* around 0.22 can be observed for sample *AP1* whereas it increases up to 0.40 for sample *AP3*, this being an additional

indication of increased disorder. Annealing experiments were performed on p-type samples deposited at high [B]/[Si] ratios (5% (*AP4*) and 10% (*AP3*)) following those results obtained at low doping concentration (*AP1*). Unfortunately, these samples suffered from peeling off problems, probably associated to increased stress in the material due to an excessive concentration of boron atoms. Moreover, the rapid effusion of hydrogen in this case seemed to be responsible for the cracking of the surface.

Secondary Ion Mass Spectrometry (SIMS) measurements were also performed on samples under study. A boron solid phase concentration around 3×10^{21} cm^{-3} was obtained in sample *AP3*. Nevertheless, this sample exhibited a very disordered structure due to an excessive incorporation of boron atoms into the amorphous network. As shown above, annealing treatments revealed that improved electrical properties could be obtained after submitting the samples to relatively moderate temperatures (< 375ºC) when dealing with [B]/[Si] ratios of 1% in gas phase (*AP1*). In this case, SIMS measurements resulted in boron solid phase concentrations around one order of magnitude lower ($\sim5\times10^{20}$ cm^{-3}) than that of *AP3* material, fact that led to a much ordered material as seen in PDS spectra.

In summary, p-type doping of a-Si:H was proved to be a complicated process. Comparable conductivities to those typically reported in PECVD-obtained material could only be achieved after using very high [B]/[Si] ratios in gas phase or after performing annealing treatments. Additional experiments carried out at different hydrogen dilutions (not presented here) manifested a decrease in the solid phase incorporation of boron as more hydrogen was added to the mixture [Villar et al. 2004]. In that sense, the high ability of Hot-Wire CVD to produce atomic hydrogen (when compared with PECVD) might account for the need of higher [B]/[Si] ratios in gas phase.

5.3.2. p-type nc-Si:H

As mentioned earlier, p-type nc-Si:H samples have been proposed as an alternative to p-type a-Si:H due to its high electrical conductivity and low optical absorption in the short wavelength region. In Table 5.4, the deposition conditions for two p-type samples exhibiting different crystalline fractions are presented. Sample *CP1* was deposited under selected deposition conditions leading to acceptable nanocrystalline intrinsic material,

whereas *CP2* was deposited with a lower gas-phase boron concentration and optimised deposition conditions to obtain higher crystallinity [Voz et al. 2000b].

Sample	T_s (ºC)	T_f (ºC)	*P (mbar)*	ϕ_{SiH4} (sccm)	D_H (%)	*[B]/[Si] (%)*
CP1	*175*	*1740*	7.0×10^{-3}	*2*	*89*	*1.6*
CP2	*125*	*1740*	1.0×10^{-2}	*4*	*93*	*0.8*

Table 5.4. *Deposition conditions for p-type doped nc-Si:H. [B]/[Si] refers to the atomic ratio in gas phase.*

Raman spectra for both samples can be seen in Fig. 5.11, where the contribution at 520 cm^{-1} evidences the crystalline fraction. In fact, this contribution was dominant for sample *CP2*, resulting in $X_c \sim 0.65$. On the other hand, a X_c value around 0.17 was obtained for sample *CP1*, which exhibited a higher amorphous phase contribution (centred at 480 cm^{-1}).

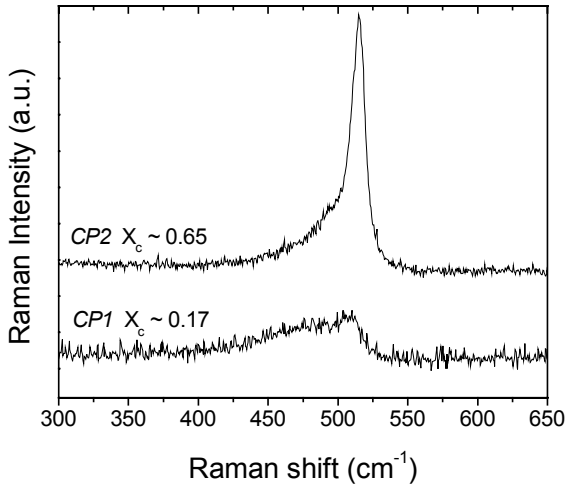

Figure 5.11. *Raman spectra for p-type nc-Si:H showing different degrees of crystallinity.*

As far as electrical properties are concerned, the Arrhenius plots of σ corresponding to p-type nc-Si:H samples are shown in Fig. 5.12. σ_d values of ~ 0.7 and ~ 1.7 $\Omega^{-1}cm^{-1}$, both satisfying the requirements for its incorporation in photovoltaic devices, were obtained for samples *CP1* and *CP2* respectively. Besides, E_A values of 0.06 and 0.03 eV were achieved for *CP1* and *CP2*, these values being also suitable for standard p-type nc-Si:H.

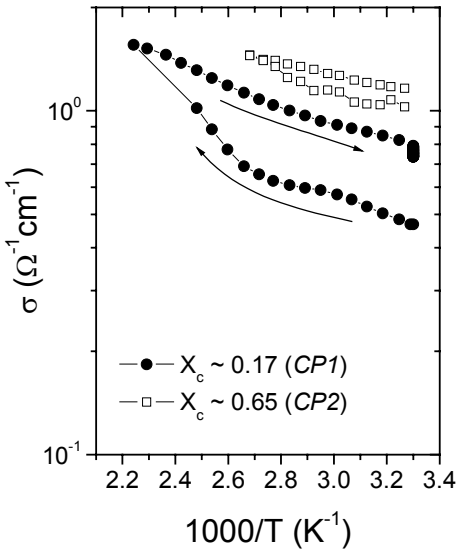

Figure 5.12. *Arrhenius plot of p-type nc-Si:H layers exhibiting different crystalline fractions: X_c ~ 0.17 (●) and X_c ~ 0.65 (□). The activation energy (E_A) was determined from the cooling part of the plot.*

All p-type layers presented so far were quite thick (d $\geq$ 0.3 μm), although thinner layers are required in photovoltaic devices as low light absorption is desired in the front contact. The necessity for thinner p-type layers is especially critical for nc-Si:H material, as the amorphous incubation phase that might limit its electrical properties has to be minimised. Consequently, layers with thicknesses around 50 nm were also deposited and analysed. Thin p-type nc-Si:H with σ_d values above 2 $\Omega^{-1}cm^{-1}$ and E_A around 0.02 eV could be obtained after properly changing some of the deposition parameters. Thus, D_H was increased up to 96% and [B]/[Si] was varied to 5%. These conditions led to the absence of any significant amorphous incubation layer and to good electrical properties, making the very thin layers suitable for their implementation in solar cells.

5.3.3. p-type a-Si:H vs. p-type nc-Si:H

The ability to grow both p-type a-Si:H and nc-Si:H by Hot-Wire CVD has been demonstrated in sections *5.3.1* and *5.3.2*. nc-Si:H samples showed electrical properties fully comparable to those typically achieved by means of PECVD. On the other hand, poorer properties were obtained for a-Si:H deposited at low substrate temperatures if a

similar [B]/[Si] ratio was maintained. An increase of [B]/[Si] led to p-type a-Si:H layers comparable to those deposited by PECVD, although some drawbacks might arise from the use of such large [B]/[Si] ratios, namely, boron diffusion into the intrinsic layer or contamination of the n-type material due to memory effects in the doped material reactor.

From the above-mentioned observations, it seemed clear that p-type nc-Si:H should be implemented in our solar cells, though some drawbacks are also linked to its use. Thus, back diffusion issues resulting from the band offset between p-type nc-Si:H and intrinsic a-Si:H affect the carrier transport and, eventually, limit the current of the device [Chatterjee et al. 1998]. Different strategies have been proposed to overcome this problem. In particular, it can be partially solved by suitably adding a very thin p-type (or even intrinsic) a-Si:H layer between the heavily doped p-type nc-Si:H and the active layer. The resulting double-layer structure can block electrons back diffusing from the intrinsic layer, thus leading to higher currents. As we will see in the next chapter, different strategies were studied in this work by combining the potential of both p-type a-Si:H and nc-Si:H layers.

5.4. Substrate influence

Intrinsic silicon thin films obtained close to the transition between nanocrystalline and amorphous growth have been proved as especially suitable when applied to photovoltaic devices obtained by Hot-Wire CVD [Klein et al 2002]. As already seen in *Chapter 3*, the microstructure of silicon thin films can be drastically varied by slight changes in the deposition parameters, namely, filament temperature, pressure or hydrogen dilution. Moreover, the above-mentioned transition has been proved to depend also on the properties of the substrate for both PECVD and Hot-Wire CVD [Kondo et al. 1996, Klein et al. 2002, Fonrodona 2003]. Similarly, the properties of doped layers are also expected to depend on the substrate.

Results presented in section *5.3* dealt with the properties of both n- and p-type layers deposited on glass, whereas doped layers are actually grown on different substrates when applied to solar cell structures. In that sense, different solar cell configurations require controlled growth of both p- and n-type layers on different substrates, thus making it necessary to evaluate the influence of the substrate properties on the doped material

characteristics. *p-i-n* devices are usually deposited onto TCO, whereas *n-i-p* cells are commonly grown on metallic substrates. The influence of the substrate might be dramatic when deposition conditions approach those leading to the transition between a-Si:H and nc-Si:H, so the study of that region of parameters becomes fundamentally interesting, even though results observed might not be straightforwardly transferred to our devices due to varying architectures and/or substrates.

Results concerning the deposition of both p- and n-type layers with thicknesses around 100 nm and growth conditions close to the transition zone will be described. Samples were simultaneously grown onto Corning 1737 glass, stainless steel (SS) and ZnO:Al coated glass under the deposition conditions listed in Table 5.5.

	T_s (ºC)	T_f (ºC)	P (mbar)	([P or B])/[Si](%)	D_H (%)
n-type	*200*	*1700*	3.0×10^{-2}	*1 (P)*	*85 - 96*
p-type	*125*	*1700*	3.0×10^{-2}	*5 (B)*	*85 - 96*

Table 5.5. *Deposition parameters for samples deposited in the substrate influence study. [dopant]/[Si] refers to the atomic ratio in gas phase.*

The dissociation of the gases was achieved by means of an inverted basket shaped Ta filament, which led to r_d values between 5 and 8 Å/s depending mainly on D_H. The evolution of structural and electrical properties as a function of D_H and the substrate nature will be next presented.

5.4.1. Structural properties

The crystallinity of the samples under study was determined by means of Raman spectroscopy. The evolution of X_c as a function of D_H and substrate for both p- and n-type samples can be observed in Fig. 5.13. As far as n-type layers are concerned, SS seemed to promote crystalline growth, whereas glass and ZnO:Al coated glass exhibited a similar trend. A D_H value of approximately 85% was necessary for all substrates in order to reach a measurable crystalline fraction. However, X_c values obtained for samples deposited onto SS remained higher than those observed on both glass and ZnO:Al coated glass for all

dilutions considered. On the other hand, X_c values for p-type samples exhibited a different behaviour. Under the present deposition conditions, higher D_H values (≥95%) were necessary for p-type layers than those needed for n-type samples to reach a measurable crystalline fraction. Furthermore, and contrary to the results obtained with n-type layers, higher X_c was observed for samples grown on glass. In fact, X_c values could be detected on glass for those layers obtained at D_H = 95%, whereas D_H ~ 96% was necessary to observe any crystalline fraction for samples deposited on either SS or ZnO:Al coated glass.

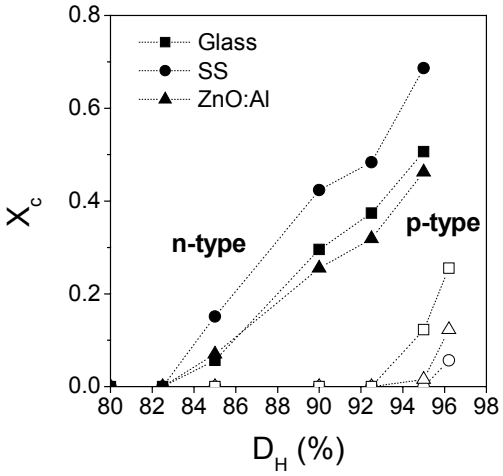

Figure 5.13. *X_c for p- and n-type layers deposited simultaneously onto different substrates as a function of D_H.*

5.4.2. Electrical properties

Coplanar dark conductivity at room temperature (σ_d) was measured for samples deposited on glass for both p- and n-type layers. The evolution of σ_d as a function of D_H can be observed in Fig. 5.14, where the a-Si:H/nc-Si:H transition can be clearly observed. σ_d for n-type layers deposited at D_H values below 85%, which were clearly amorphous, exhibited typical values for amorphous layers (between 10^{-4} $\Omega^{-1}cm^{-1}$ and 10^{-3} $\Omega^{-1}cm^{-1}$). Moreover, a typical a-Si:H σ_d value was measured at D_H = 85% in spite of its detectable crystalline fraction (X_c ~ 0.06 as seen in Fig. 5.13). Thus, coplanar conductivity seemed to be mainly controlled by the amorphous tissue surrounding the crystallites. On the other hand, n-type samples grown at D_H above 90% presented σ_d values between 2.3 and 4 $\Omega^{-1}cm^{-1}$, which are characteristic of doped nc-Si:H. This result indicated that the crystalline fraction was

important enough in this case as to determine σ_d. Moreover, E_A values between 0.06 and 0.10 eV were measured for these layers from the Arrhenius plots of σ.

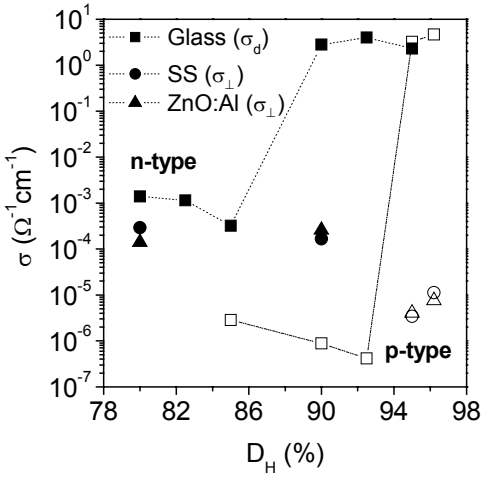

Figure 5.14. *Electrical properties at room temperature for n- and p-type layers. Glass measurements refer to coplanar (standard) conductivity (σ_d), whereas SS and ZnO:Al measurements were performed in the direction perpendicular to the substrate ($\sigma_\perp$).*

As far as p-type layers are concerned, D_H above 95% was necessary to reach σ_d values corresponding to those typically observed in nc-Si:H. X_c for those samples was higher than 0.1, which seemed to be large enough to allow the crystalline phase to determine the electrical properties of the sample in the coplanar direction, similarly to results presented in section 3.2. σ_d values between 2.2 and 4.6 $\Omega^{-1}cm^{-1}$ were obtained for samples deposited at D_H = 95% and 96% respectively. Accordingly, these samples exhibited typical p-type nc-Si:H E_A values of 0.05 and 0.03 eV respectively. On the other hand, σ_d exhibited typical a-Si:H values for low D_H, with values decreasing (between 2×10^{-6} and 3×10^{-7} $\Omega^{-1}cm^{-1}$) when approaching the transition to nc-Si:H.

Both structural and electrical properties clearly indicated that higher D_H was needed for p-type layers than for n-type ones to reach nc-Si:H properties. The high diborane concentration ([B]/[Si] = 5% in gas phase) seemed to be responsible for this behaviour. It is known that diborane tends to increase the amorphous character of deposited samples [Peiró et al. 1998]. Regarding the σ_d evolution (Fig. 5.14), a similar trend could be

observed for both p- and n-type amorphous samples. Thus, samples deposited just before the transition to nc-Si:H (D_H = 85% for n-type and D_H = 92% for p-type layers) exhibited the lowest σ_d, while it slightly increased as D_H was lowered. This result could be attributed to a worsening of the a-Si:H properties as the deposition conditions approached those leading to nc-Si:H. This result could be provoked by an increase in the structural disorder and in the porosity of deposited samples.

Measurements performed in the direction perpendicular to the substrate on those samples deposited onto SS and ZnO:Al coated glass allowed us to obtain some information on the properties of the doped layers and the corresponding interfaces. Current vs. voltage curves were measured to analyse the electrical properties and four probes were used to minimize those effects arising from the electrode-probe contact. A schematic view of the geometry used can be seen in Fig. 5.15.

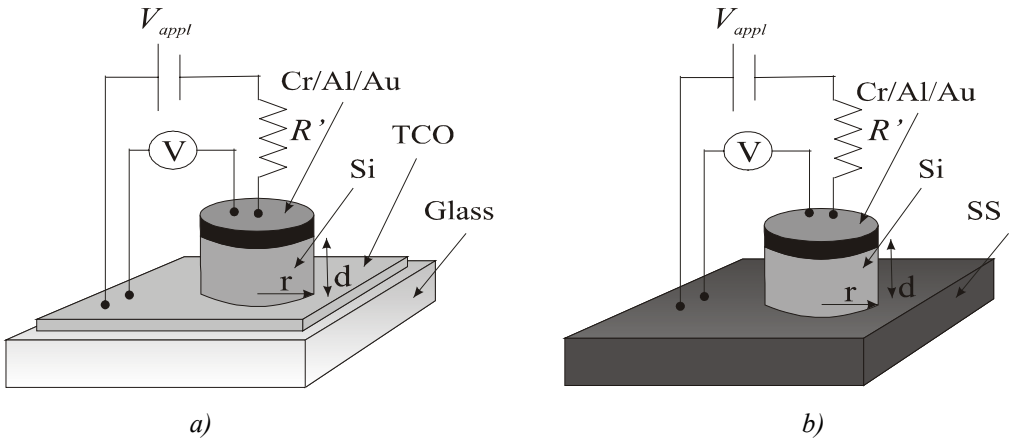

Figure 5.15. *Electrical measurements in the direction perpendicular to the substrate for doped layers deposited on ZnO:Al coated glass (a) or stainless steel, SS (b).*

Samples were dry-etched with a plasma of CF_4 diluted into oxygen (20%) at a process pressure of 0.4 mbar and RF power of 15 mW/cm^2. Voltage vs. current measurements were performed between –25 and +25 mA/cm^2, so that standard conditions under which solar cells operate could be evaluated.

The voltage vs. current curves exhibited a linear behaviour for both p- and n-type samples on both SS and ZnO:Al coated glass regardless its crystalline fraction. This result pointed out the ohmic behaviour of the junctions. This fact allowed us to determine the resistance (*R*), from which the conductivity in the direction perpendicular to the substrate ($\sigma_\perp$) could be evaluated under the assumption of homogeneous conductivity without any effect from the interfaces. Some of the results obtained can be also observed in Fig. 5.14. It is very important to remark that $\sigma_\perp$ was calculated under the assumption of homogeneous conductivity, which, as we will see next, might not be satisfied.

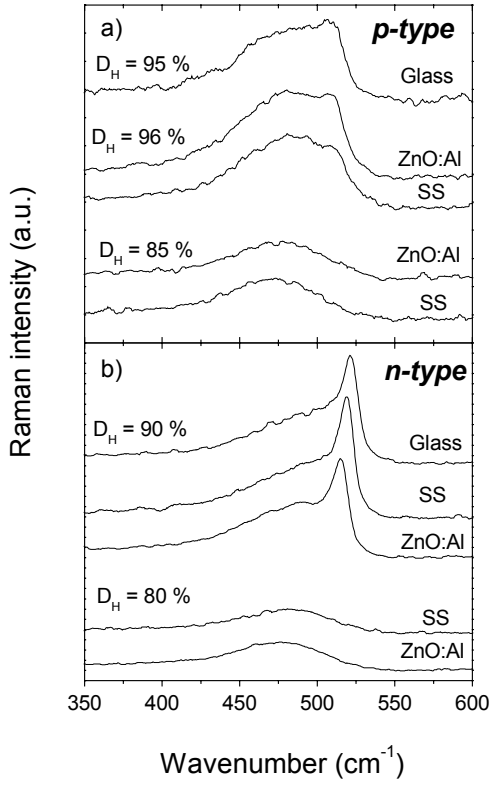

Figure 5.16. *Raman spectra for p- (a) and n-type (b) layers deposited on different substrates at varying hydrogen dilutions.*

Presented results showed that the electrical properties of both p- and n-type samples clearly depended on the measurement direction, even for samples exhibiting similar structural features. Raman spectra for the p-type sample deposited on glass at D_H = 95% and those grown on SS and ZnO:Al coated glass at D_H = 96% are plotted in Fig. 5.16(a). Although structural features, as observed in the figure, remained similar, clearly different electrical

properties in different directions were achieved. Thus, σ_d measured on glass presented a typical value for nc-Si:H, whereas $\sigma_\perp$ measured on both SS and ZnO:Al coated glass exhibited a value approximately five orders of magnitude lower, which was close to the σ_d value obtained for amorphous samples. Similar behaviour was observed for the n-type layers grown at D_H = 90% (Fig. 5.16(b)), which also exhibited similar structural properties on all substrates. In this case, a difference of four orders of magnitude between σ_d and $\sigma_\perp$ was determined as seen in Fig. 5.14. Thus, although σ_d varied from $10^{-3}\ \Omega^{-1}cm^{-1}$ to $\sim 2\ \Omega^{-1}cm^{-1}$ as D_H was changed from 80% (amorphous) to 90% (nanocrystalline) in agreement with the structural changes (Fig. 5.16(b)), $\sigma_\perp$ remained almost constant on both SS and ZnO:Al coated glass (Fig. 5.14).

Previous results indicated that the assumption under which $\sigma_\perp$ was calculated were not in fact satisfied. This behaviour was not unexpected, as conduction perpendicular to the substrate seemed to be mainly controlled by electrical transport at the barriers created in the junction between the semiconductor and the substrate, or at the amorphous incubation phase formed during the initial stages of growth. In that sense, electrical measurements shown in Fig. 5.14 for $\sigma_\perp$ allowed us to obtain a value for the contact resistance, which was clearly dependent on the interface properties and on the initial stages of growth. These values depended on the type of dopant. Thus, contact resistances between 1 and 3 Ωcm^2 were obtained for p-type samples, whereas n-type layers exhibited values close to 0.05 Ωcm^2. *p-i-n* solar cells usually present a TCO/p junction, whereas *n-i-p* cells can be grown on SS, for which an SS/n junction is observed. Assuming a typical current density of 20 mA/cm^2, a remarkable potential drop between 20 and 60 mV for the TCO/p junction, and a much lower drop of approximately 1 mV for the SS/n junction, were calculated.

5.5. Summary

The ability to deposit both p- and n-type doped layers by means of Hot-Wire CVD after the addition of B_2H_6 and PH_3 respectively was demonstrated. n-type material was obtained in a relatively straightforward manner, as similar conditions to those leading to our state-of-the-art intrinsic a-Si:H could be employed. An atomic ratio ([P]/[Si]) of 1% was used leading to acceptable electrical properties ($\sigma_d > 10^{-3}\ \Omega^{-1}cm^{-1}$ and $E_A < 0.3$ eV), which allowed the

incorporation of this material in photovoltaic devices. On the other hand, the deposition of p-type a-Si:H material proved to be more complicated, as those conditions leading to our best intrinsic a-Si:H did not result in satisfactory material. Thus, low σ_d (~ 10^{-6} $\Omega^{-1}cm^{-1}$) was obtained when typical [B]/[Si] ratios between 1 and 2% were employed. Nevertheless, two alternative approaches allowed the growth of p-type layers with acceptable features. Thus, both the annealing of the samples and the utilization of very high doping ratios (~10%) led to satisfactory σ_d and E_A values.

The excessive concentration of hydrogen in the material (C_H ~ 16%) might be responsible for the behaviour observed in p-type layers. Boron atoms are known to form boron-hydrogen complexes, which can be removed after increasing the temperature, thus favouring the release of hydrogen and allowing the boron atoms to effectively contribute to the doping of the material. On the other hand, the use of [B]/[Si] ~ 10% seemed to allow a sufficient number of boron atoms to effectively dope the material despite the formation of B-H complexes, although in this case the large amount of B atoms resulted in too disordered material. Additionally, p-type nc-Si:H was also deposited combining both high conductivity and low optical absorption. In this case, suitable electrical properties ($\sigma_d > 2\ \Omega^{-1}cm^{-1}$ and $E_A < 0.02$ eV), even for thicknesses below 50 nm, were obtained after tuning the growth conditions.

Doped layers are grown on different substrates when applied to solar cell structures, so that the substrate influence on the doped layers properties had to be carefully analysed. In particular, the region close to the transition between a-Si:H and nc-Si:H was studied. Our results showed that stainless steel promoted crystalline growth when n-type layers were considered, whereas enhanced crystallinity on glass was achieved for p-type material. Moreover, the electrical properties in the direction perpendicular to the substrate were mainly determined by the junction properties, which were clearly better for the n-type material than for the p-type one. In fact, measured results show that TCO/p junctions are expected to induce a detectable voltage drop when incorporated in photovoltaic devices.